Deriving exclusion maps from C-band SAR time-series in support of floodwater mapping

Jie Zhao[1,2,3,*], Ramona Pelich[1], Renaud Hostache[1], Patrick Matgen[1], Senmao Cao[4], Wolfgang Wagner[2], Marco Chini[1]

[1] Department of Environmental Research and Innovation, Luxembourg Institute of Science and Technology, 5 Avenue des Hauts-Fourneaux, 4362, Esch-sur-Alzette, Luxembourg-(jie.zhao, ramona.pelich, Patrick.matgen, Renaud.hostache, marco.chini)@list.lu

[2] Research Group Remote Sensing, Department of Geodesy and Geoinformation, Vienna University of Technology, 1040, Vienna, Austria – wolfgang.wagner@geo.tuwien.ac.at

[3] Centre for Water Resource Systems, Vienna University of Technology, 1040, Vienna, Austria

[4] EODC Earth Observation Data Centre, 1030, Vienna – senmao.cao@eodc.eu

Abstract:

Synthetic Aperture Radar (SAR) intensity is used as an input to many flood-mapping algorithms. The appearance of floodwater tends to cause a substantial decrease of backscatter intensity over scarcely vegetated terrain. However, limitations exist in areas where the SAR backscatter is not sufficiently sensitive to surface changes, e.g. shadow areas due to topography or obstacles on the ground, densely forested areas, sand, etc. Thus, we argue that it is of paramount importance to complement any SAR-based flood extent map with an exclusion map (EX-map) indicating all areas where the presence of water cannot be derived from SAR intensity observations. In

* Corresponding author.
Email address: jie.zhao@list.lu (J.Zhao)

this study, we introduce a methodology for generating an EX-map based on the analysis of time-series of SAR backscatter data. In particular, the identification of the EX-map is based on the combined use of three temporal indicators based on backscatter statistics, i.e. temporal median, minimum and standard deviation. As a test case, EX-maps were derived from Sentinel-1 data acquired during the 2014-2019 time period from six representative study sites. Reference maps were generated using a global land cover map, Digital Elevation Model (DEM)-derived shadow/layover masks, global urban footprint (GUF) data and a Sand Exclusion Layer (SEL). The cross-comparison revealed that the EX-map was consistent with reference maps obtained from other data sources.

Keyword: Sentinel-1, flood risk management, time series analysis, SAR, EX-map (*exclusion map*)

1. Introduction

Flooding is a major hazard in both rural and urban areas worldwide, leading to significant human and economic losses (CRED UNISDR, 2015). Flood mapping plays a central role in emergency response, relief and post-disaster reconstruction, as well as in disaster risk financing. For several years, Synthetic Aperture Radar (SAR) data have been widely used for this purpose because active microwave measurements are highly sensitive to the presence of surface water, regardless of the sun illumination and weather conditions. SAR-based algorithms enabling automatic floodwater mapping have reached a certain degree of maturity for bare soils and sparsely vegetated areas (e.g. Chini et al., 2017; Debusscher and Van Coillie, 2019; Landuyt et al., 2019; Li et al., 2018; Liang and Liu, 2020; Natsuaki and Nagai, 2020; Schlaffer et al., 2015; Zhao et al., 2019) where the appearance of floodwater often results in a substantial drop in SAR backscattering. Generally, open calm water leads to a low backscatter when compared with surrounding land surfaces (Ulaby and Long, 2014). However, detecting surface water in vegetated and urban areas remains challenging. In vegetated areas, Pierdicca et al., (2018) and Tsyganskaya et al., (2018a) emphasized the possibility of exploiting an enhancement of the double-bounce mechanism (i.e. multiple reflections from the horizontal surface and the vertical structures) caused by the presence of water under the vegetation. Methods exploiting this behaviour require the SAR signal to penetrate the canopy and reach the ground. Moreover, the mapping of floodwater in urban areas has improved in recent years because of new methods exploiting the InSAR multitemporal coherence from single look complex data (Chini et al., 2019; Li et al., 2019b; Pulvirenti et al., 2021, 2016). Applications of such methods have shown that the frequently observed under-detection of floodwater in built-up environments could be significantly reduced when compared with more conventional flood mapping methods based only on SAR intensity.

There are other land cover classes and topographic conditions where the detection of floodwater using SAR intensity is impeded, e.g. shadow areas caused by topography or obstacles on the ground (e.g. buildings) hindering the signal to sense the surface. Some land cover classes, such as layover areas, dry sand (Martinis et al., 2018), tarmac and building areas (Giustarini et al., 2013), in principle, allow the surface to be sensed but the backscattering variations caused by the presence of water becomes insignificant when compared with the normal “unflooded” condition.

Nowadays, a majority of methods mentioned above generate binary flood extent maps with two classes identified: flooded and non-flooded pixels (e.g. Chini et al., 2017, 2019; Cian et al., 2018; Li et al., 2019; Shen et al., 2019; Tsyganskaya et al., 2018a). Several probabilistic flood mapping approaches have been developed to provide uncertainty information complementing the flood extent maps (e.g. Giustarini et al., 2016; Schlaffer et al., 2017; Westerhoff et al., 2013). We argue that one important piece of information that is still missing is maps of areas where the SAR signal is insensitive to surface changes. In such areas, floodwater cannot be mapped with currently available input data and retrieval algorithms, and this information should be available to any user of SAR-derived flood extent maps. For example, this is a crucial piece of information when responding to an emergency or for mitigating flood impacts (Matgen et al., 2019). Such complementary information also has high value when integrating observations of flood extent into flood prediction models. Indeed, SAR-derived flood extent maps are frequently taken into account when calibrating, evaluating and updating flood inundation models (e.g., Wood et al., 2016, Hostache et al., 2018). However, as shown in Di Mauro et al., (2021), errors in satellite-derived flood extent maps may lead to a degradation of model forecasts when such areas are not clearly identified a priori. It is therefore of primary importance to identify all insensitive areas that are potentially responsible for large observation biases that may render assimilation filters inefficient.

To our knowledge, so far only a few studies have addressed the problem of identifying such insensitive areas. Depending on the type of data considered, these studies can be classified into two main categories: those making use of ancillary data, e.g. DEM / DSM and Height Above Nearest Drainage (HAND) (Nobre et al., 2011) and those based solely on the analysis of SAR data. In order to reduce the floodwater over-detection and to improve the accuracy of flood maps, shadow/layover areas caused by topography derived from a 30m SRTM DEM were applied in Benoudjit and Guida, (2019) and Mason et al., (2018). Huang et al., (2017) compared the ability of two DEM-based terrain indices (i.e. the Multi-resolution Valley Bottom Flatness (MrVBF) and HAND) to remove the shadow areas in Sentinel-1 based surface water maps. To extract the same mask for buildings and tall vegetation, LiDAR DSMs with metric spatial resolution were used (Mason et al., 2018). However, the lack of high-resolution DSMs at global scale often hampers the generation of shadow/layover masks at the resolution of the SAR data (Chen et al., 2018). HAND-derived masks were also applied to reduce over-detection in hills and mountain areas (Zhao et al., 2021). Land use maps were considered in order to exclude man-made infrastructures and urbanized areas from the investigated areas (Grimaldi et al., 2020). With respect to SAR intensity-derived exclusion masking, only two studies are currently available in the scientific literature. Martinis et al., (2018) introduced the Sand Exclusion Layer (SEL) in order to deal with arid areas characterized by permanent low backscattering values that might be misclassified as water bodies. By analysing a time series of backscatter obtained from Sentinel-1, all pixels having at least half of the time backscattering values below -15 dB are included in the SEL. Another study identified pixels that are not sensitive to surface changes in the framework of SAR-based soil moisture retrievals (Bauer-Marschallinger et al., 2019). The authors generated a sensitivity mask in order to identify regions with unreliable Sentinel-1-based surface soil moisture retrievals (SSM). Their mask includes pixels with a low sensitivity of Sentinel-1 C-band signals to soil moisture variations. The mask mainly includes pixels representing cities and urban settlements. However, we argue that a sensitivity mask designed for 500 m resolution SSM products is not adequate for masking high to medium-resolution SAR-based flood extent maps such as those derived from 20 m resolution Sentinel-1 images. The main reason for this is due to the fact that land cover classes at various spatial resolution are recorded differently from a SAR sensor.

As shown by the above-mentioned studies, there are already several masks available. However, these were defined to exclude specific regions (e.g. shadow/layover, hills/mountains, sand, urban areas) and designed for specific applications (e.g. water body mapping, soil moisture retrievals). When it comes to SAR intensity-based approaches for detecting surface changes, such as those related to floodwater, we argue that a comprehensive and exhaustive mask including all insensitive areas is still missing. In this paper, we therefore aim to develop and evaluate a method to extract such a comprehensive "exclusion" map (EX-map) with several sublayers. It shall identify all pixels that cannot be reliably classified as 'flooded' or 'not flooded' using SAR intensity data. We argue that such an accompanying information layer would support any flood mapping activity since it would provide critical information enabling a more efficient and reliable exploitation of the data. Additionally, the EX-map could also be used in many other applications aiming to measure SAR backscattering changes over time, for example in the context of soil moisture retrievals. We hypothesize that an orbit-specific EX-map can be obtained through time series analyses of Sentinel-1 C-band SAR data acquired from the same orbit. To avoid discrepancies due to the combination of various sources of EO data, the proposed EX-map shall be derived from the same data source as the one used for floodwater mapping. Thus, the TU Wien Data Cube is a good option for obtaining masks where Sentinel-1 cannot detect floods for physical reasons (Wagner et al., 2020). In our study, the proposed method is tested on stacks of Sentinel-1 intensity data from Data Cube at 20m resolution acquired from different AOIs located in various areas across the globe.

The paper is organized as follows: Section 2 describes the multi-temporal indices employed for deriving the exclusion map and the proposed algorithm. Next, Section 3 introduces six case studies~~,~~ located in Europe, Africa, Asia and North America and their associated datasets. The results are presented and discussed in Section 4 and the application of the EX-map is shown in Section 5. Finally, conclusions and an outlook to ongoing and future studies are provided in the final section.

2. Methodology

In this study, we introduce EX-map as an ensemble of pixels that cannot be classified as ‘flooded’ or ‘not flooded’ using SAR intensity observations. Thus, the map is specific to a particular signal wavelength and acquisition geometry (i.e. orbital track). It contains pixels belonging to different land cover classes and different SAR geometrical distortions preventing the classification of floodwater. In this section, the EX-map classification method is described.

We first present the features proposed to generate the EX-map and explain how these features are used to derive the EX-map.

2.1. EX-map generation

2.1.1. Rationale

The proposed method relies on the following working hypothesis: When mapping floodwater using only the intensity information in SAR imagery, areas characterized by permanently low and high backscattering values, as well as areas characterized by stable backscattering over time should be excluded from further analysis. The following sections provide details and explanations on this assumption.

Low backscattering (LB) is typical of i) smooth surfaces, e.g. water bodies, tarmac, where the specular reflection dominates the entire surface scattering field; ii) land cover classes absorbing the impinging signal, e.g. very dry surfaces like sand, wet snow, grassland; iii) areas in the shadow of obstructing objects, e.g. shadows caused by high trees, mountains and buildings. Such areas prevent the detection of floodwater using single-image, dual-image or even time-series methods because the backscattering in the flooded and unflooded conditions shows similarly low values. We aim for the exclusion of permanent water-lookalike classes and stable objects over time because excluding pixels with only temporarily low backscattering values such as wet snow or specific types of vegetation, e.g. crops, would increase the risk of excluding potentially flooded areas. As a consequence, the proposed EX-map is expected to include pixels exhibiting only permanently low backscatter, such as permanent water, smooth tarmac, shadow and sandy areas.

High backscattering (HB) is typical of urban and steep areas, where foreshortening, layover and double-bounce develop as a result of the particular geometrical arrangement between the sensor Line-of-Sight (LoS) and the object class structure (Ferro et al., 2011; Franceschetti et al., 2002). In particular, when it comes to urban areas, the increase in backscattering caused by the presence of water is hardly detectable. In fact, the increase of the double-bounce backscatter is mainly related to the geometric arrangement of the SAR LoS and the building facades while sensitivity to increasing backscatter caused by floodwater is relatively low (Pulvirenti et al., 2016).

Stable backscattering (SB) is a characteristic area where backscattering remains stable regardless of surface conditions. The previously mentioned low and high backscattering areas may also fall into this category. However, permanent water bodies, albeit characterized by consistently low backscatter values, do not necessarily belong to this behavioural class because rain or wind occasionally change the roughness of the water surface, thereby causing temporarily high backscatter values. Land cover classes expected to belong to this class are densely vegetated areas (e.g. dense forests), where the SAR signal hardly penetrates the vegetation canopy and does not reach the ground. It should be noted that the canopy penetration capability of SAR signals depends on their wavelength, as well as the orbit path, i.e. the incidence angle.

Based on this description of the SAR backscattering classes constituting the EX-map, we argue that in theory the SB class should include the other two classes (i.e. HB and LB). These classes tend to produce stable backscatter over time, with the notable exception of water bodies. It is worth highlighting that each land cover class has its own speckle magnitude rendering it difficult to accurately define "temporal stability" for all land cover classes. As a consequence, the proposed strategy is to first classify LB and HB classes, which have rather singular backscatter values. Next, we can identify the SB class by analysing the stability for the remaining areas. Therefore, the EX-map is the union of the LB, HB and SB classes. It is worth mentioning that LB and SB, as well as HB and SB, are expected to partially overlap. Here we assume that the targeted EX-map is expected to include the following SAR-based categories: (1) permanent water bodies; (2) shadow (topographic, urban) and arid areas; (3) layover (topographic); (4) layover/double-bounce (urban); (5) densely vegetated areas.

2.1.2. Feature extraction

In order to map areas with very low and high backscatter, several texture features can be considered. For instance, the local Getis-Ord G_i has already been successfully used as an indicator of spatial autocorrelation to identify built-up areas (Gamba et al., 2009), to support crowdsourced-based flood detection (Panteras and Cervone, 2018), to identify hotspots on freeways (Songchitruksa and Zeng, 2010) and to analyse land surface temperature (Tran et al., 2017). It is a powerful technique for characterizing and quantifying the spatial autocorrelation of remotely sensed imagery, providing a measure of spatial dependence of neighbouring pixels (Tran et al., 2017; Wulder and Boots, 1998). Generally, the local Getis-Ord G_i (Getis and Ord, 1992; Ord and Getis, 1995) is used to identify outliers. The technique allows the identification of the presence of hot spots (i.e. clusters of high values) and cold spots (i.e. clusters of low values) over an entire area by looking at the feature of interest, e.g. backscatter values. More specifically, layover (topographic) and layover/double-bounce (urban) with extremely high backscatter can be regarded as hot spots in SAR scenes, while permanent water bodies, shadow (topographic, urban) and arid areas characterized by extremely low backscatter can be considered as cold spots in SAR images. The standardized local Getis-Ord G_i statistic is defined as (Getis and Ord, 1992; Ord and Getis, 1995):

$$G_i = \frac{\sum_{j=1}^{n} w_{i,j} x_j - \bar{X} \sum_{j=1}^{n} w_{i,j}}{S\sqrt{\frac{n\sum_{j=1}^{n} w_{i,j}^2 - \left(\sum_{j=1}^{n} w_{i,j}\right)^2}{n-1}}} \quad (1)$$

$$\bar{X} = \frac{\sum_{j=1}^{n} x_j}{n} \quad (2)$$

$$S = \sqrt{\frac{\sum_{j=1}^{n} x_j^2}{n} - (\bar{X})^2} \quad (3)$$

where

x_j = the value of variable x at location j

n = the total number of image's pixels

In this study, the weight matrix $w_{i,j}$ is set with a distance lag d=1 and associations follow the so called "queen's case", i.e. all pixels adjacent to x_j are considered. The spatial resolution of the local Getis-Ord G_i image decreases when d increases. Thus, we chose d=1 to keep the spatial resolution as high as possible. High positive local Getis-Ord G_i identifies clusters of high values (i.e. hot spots), while low negative local Getis-Ord G_i represents clusters of low values (i.e. cold spots). Here, we propose to apply local G_i to the temporal median backscattering value derived from a stack of SAR images in order to classify the LB and HB classes, respectively. We argue that local G_i has the advantage of providing backscattering information that is normalized with respect to the local land cover classes in each image. This is to be preferred over an absolute indicator that may substantially vary from one image to another, as the backscatter value depends on several factors, such as the incidence angle and the LoS. Thus, local G_i mitigates differences in the backscattering values of different classes due to differences in acquisition geometry, enabling us to characterize LB and HB in a more robust and systematic way. This is visible in Figure 1, where it is possible to appreciate how the temporal median backscattering largely depends on the test site, while the local G_i is less affected. This is more evident for layover (topographic) and layover/double-bounce (urban) classes, where the dependence on the incidence angle is very strong. It is worth considering that the local G_i used here not only takes into account the spatial characteristics of classes but also provides information on their temporal behaviour since it is calculated from the temporal median of the backscattering.

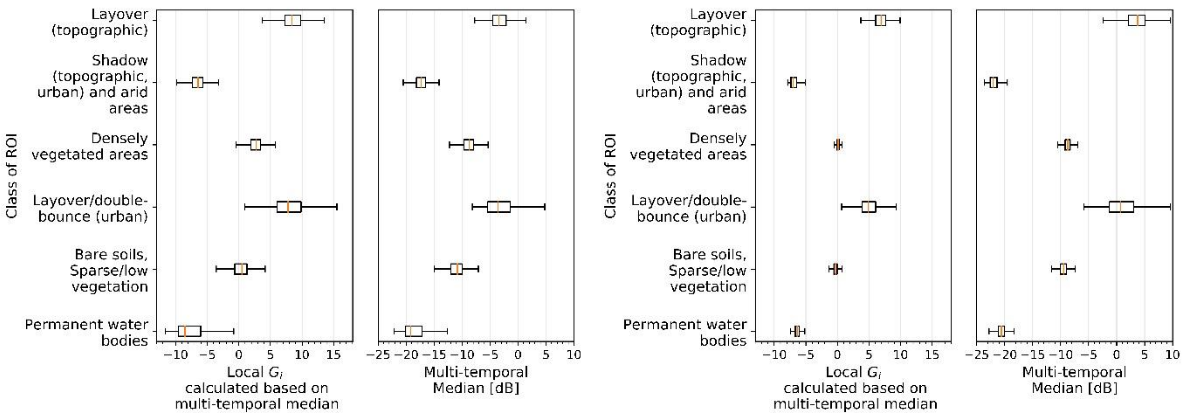

(a) Manually derived ROIs covering study site 1 (Tile E040N023T1, track 30)

(b) Manually derived ROIs covering study site 2 (Tile E046N014T1, track 15)

Figure 1 Example of local G_i and multi-temporal median of different land cover classes using 215 images and 167 images, respectively.

Other multi-temporal statistical features such as the standard deviation have demonstrated their usefulness in SAR image classification (Clauss et al., 2018; Lin and Perissin, 2018). In this study, we make use of the multi-temporal standard deviation (σ_{MT}) and the multi-temporal minimum (min_{MT}) to identify areas with limited backscatter variations, i.e. densely vegetated areas, which could be confused with bare soils, sparse/low vegetation if both indexes were not used.

To show the effectiveness of the three proposed indices for identifying the LB, HB and SB classes, their values were extracted from different classes. These include land cover classes and areas known to be affected by radar-specific imaging distortions that should be part of the EX-map, as well as land cover classes where the detection of floodwater using SAR-based intensity approaches should be possible, e.g. bare soils, sparse/low vegetation. Thus, from all test sites available, the ROIs of layover (topographic), shadow (topographic, urban) and arid areas, densely vegetated areas, layover/double-bounce (urban), bare soils, sparse/low vegetation and permanent water bodies are manually selected by visually inspecting the multi-temporal median SAR image, various landcover maps and topographic data. The extracted values shown in Figure 2 are used to analyse the effectiveness of the selected parameters for generating the EX-map. The results indicate that the local G_i is rather effective in detecting regions with low and high backscatter values, although it fails to separate densely vegetated areas from bare soils and sparse/low vegetation. Concerning the separation of these two remaining classes, we notice in Figure 2 that the different values of σ_{MT} and min_{MT} show a high ability to solve this problem.

It is worth noting that for some classes the multi-temporal standard deviations are higher than expected. This may be due to the fact that the SAR-based land cover classes cannot be fully described when considering land cover classes obtained with optical sensors. One example for this is the layover/double-bounce (urban) class, of which only the double-bounce area is of interest in our study, while the urban class from the landcover map also contains parking lots, roads/railways and vegetation/tree close to buildings, etc.

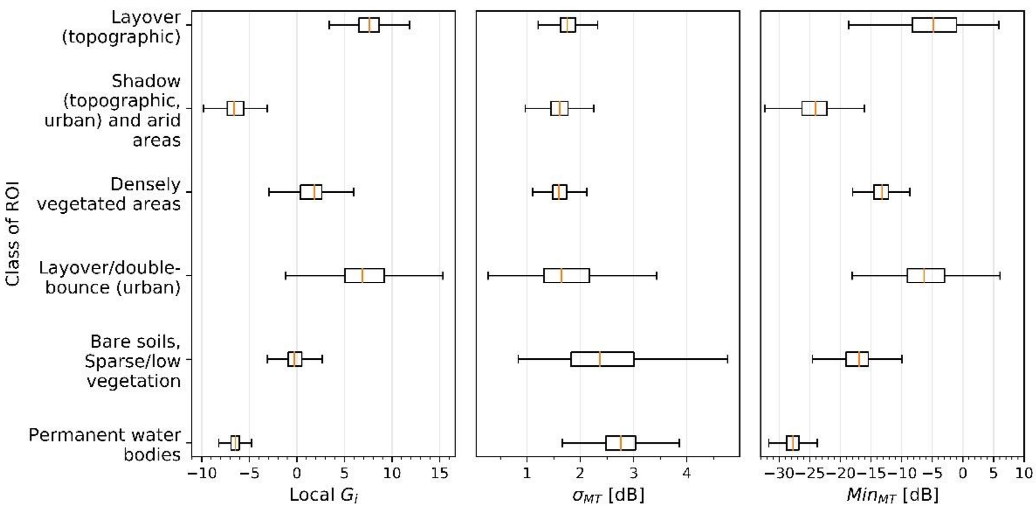

Figure 2 Example of local G_i, multi-temporal standard deviation and multi-temporal minimum of different land cover classes (ROIs are selected manually from all Sentinel-1 datasets available, which are composed of 1735 images).

2.1.3. EX-map computation algorithm

The procedure to derive the EX-map follows a decision tree approach. Since SAR backscattering of a land cover class varies with the acquisition geometry (e.g. topography, incidence angle and orbit path), adaptive approaches to select classification parameters are needed. Hence, the proposed method is to first distinguish the LB and HB classes using the local G_i map, before making use of σ_{MT} and min_{MT} to separate the SB scattering class from the areas that remained after the first classification step. The proposed procedure is composed of the following steps that are also summarized in the block diagram shown in Figure 3:

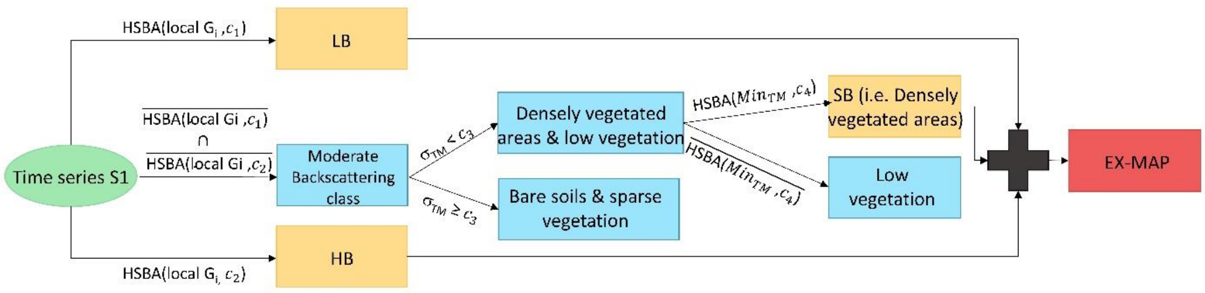

Figure 3 Decision tree using temporal indicators for EX-map extraction. The input data is shown in green, the images with mixed pixels of different land cover classes are shown in blue, the layers of the EX-map are shown in yellow and the final generated EX-map is shown in red. The c_1, c_2 and c_4 parameters are automatically selected by HSBA.

1) LB and HB usually represent a small fraction of the local G_i images and it is assumed that the distribution of LB and background and distribution of HB and background are bimodal in local G_i images. However, the identification of LB and HB classes from the entire image might be difficult because of the imbalanced proportion of pixels between LB/HB and their background. As a consequence, to identify LB and HB classes, we adopt the hierarchical split-based approach (HSBA) proposed by Chini et al., (2017). HSBA is a statistical modelling-based classification algorithm, which makes use of hierarchical image splitting, region growing and adaptive thresholding to identify a class of interest in the entire image. To identify pixels belonging to LB and HB using HSBA, we classify areas of very low and very high local G_i, respectively. HSBA is applied twice to classify the LB and HB classes separately. Firstly, HSBA hierarchically splits the local G_i image into tiles of various sizes and selects only tiles with an identifiable bimodal distribution. The selected tiles are expected to contain pixel values from the target and its background that can be modelled with bimodal Probability Density Functions (PDFs). The HSBA algorithm is fully automatic and the only parameter that needs to be set a priori is the local G_i threshold (c_1 for LB and c_2 for HB) for which the PDF of the

class of interest is expected to be below or above this value. The local G_i threshold is located between the mean values of the PDF of the classes of interest (i.e., PDF_{LB} and PDF_{HB}, respectively) and the one of the backgrounds. These local G_i thresholds are then used in HSBA to search for tiles where a robust parameterization of PDF_{LB}/PDF_{HB} is possible. Because of differences in incidence angles, the backscattering values of the classes of interest vary from one site to another: it may be that the parametrization of the PDFs is not possible using a constant c_1 and c_2. To this end, several values were tested, especially for layover (topographic) and layover/double-bounce (urban) where the backscattering varies significantly depending on the incidence angle. We tested c_1 and c_2 in the intervals [-8 : -5] and [5 : 8] with a step of one. Since the objective is to select the classes with the lowest and the highest local G_i values, we started from -8 for c_1 and 8 for c_2 and we selected the first value that allows to select tiles for parameterizing PDF_{LB} and PDF_{HB}. From the local G_i histogram corresponding to areas depicted by all selected tiles, PDF_{LB} and PDF_{HB} are finally parameterized and iterative thresholding and region growing are applied sequentially in order to identify the LB and HB classes, respectively. The threshold to select the seed for the region growing is fixed to the local G_i value where PDFs of LB (or HB) and the total histogram start diverging, while the threshold to stop region growing is fixed to the value that minimizes the root-mean-squared error (RMSE) between PDF_{LB} (PDF_{HB}) and the histogram resulting from the region growing. More details about the classification procedure can be found in Chini et al., (2017). In order to select ranges of values for the parameters c_1 and c_2, the ROIs covering LB, HB and their background classes are selected from one SAR image and for each ROI the distribution of local G_i is obtained (see example in Figure 4). It is apparent from Figure 4 that our assumption regarding a bimodal distribution of LB/background and HB/background is valid. Thus, based on the extracted values shown in Figure 4, the first guesses for c_1 and c_2 are fixed. These values are used for all test sites considered in this study.

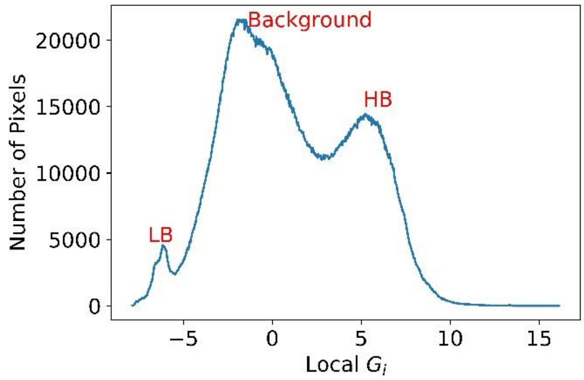

Figure 4 Example of a bimodal distribution of LB and HB areas. The histogram is derived from ROIs selected from a local G_i image (Tile E046N014T1, track 15).

2) As shown in the block diagram (Figure 3), the SB class is identified using σ_{MT} and min_{MT} following the extraction of areas with high/low local G_i. Therefore, the remaining class that needs to be identified as part of the EX-map represents the densely vegetated areas that are assumed to produce stable backscatter over time. To confirm this hypothesis, σ_{MT} over a stack of SAR images was extracted and averaged for the different land cover classes. This analysis confirms that the densely vegetated areas have the lowest σ_{MT} mean value and least dispersed σ_{MT} when compared to the other classes (Figure 2). According to Figure 2, the bare soils, sparse/low vegetation class is characterized by a higher σ_{MT} mean value and a larger range of values, thereby creating some overlap with the densely vegetated area class. Hence, low vegetation areas (i.e. vegetation with moderate and stable backscatter over time) are defined as the areas with σ_{MT} below 1.6 dB according to the median value of the densely vegetated areas class obtained from the analysis shown in Figure 2. In other words, the threshold separating densely vegetated areas and other vegetation from bare soils and sparse vegetation, i.e. c_3, is set to a value of 1.6 dB. The parameter c_3 was fixed at the same value for all test cases because backscattering from densely vegetated areas is mainly due to volumetric scattering which is less affected by differences in incidence angles. This is also evident from this land cover's reduced spread of σ_{MT} when compared with that of other classes. Considering the average of the min_{MT}

for the different land cover classes (Figure 2), densely vegetated areas have higher values of min_{MT} than bare soils, sparse/low vegetation. From this analysis, we conclude that the densely vegetated areas class is characterized by relatively low σ_{MT} and relatively high min_{MT} when compared with other classes. One could argue that selecting areas of low σ_{MT} is sufficient for mapping areas of stable backscatter. However, the probability of misclassifying areas as stable because of an insufficient image time sampling is relatively high due to a longer revisit time when compared with the change in land surface (in some areas, the revisit time of Sentinel-1 is 12 or 24 days instead of 6 days). Therefore, min_{MT} was used at the same time in order to remove low vegetation with low σ_{MT}. In the areas classified as 'densely vegetated areas and low vegetation' with low σ_{MT}, we check the distributions of min_{MT} for different classes that were included erroneously. Since the maximum number of expected classes is two, HSBA was applied to identify the class of interest, i.e. "densely vegetated areas". As for the LB and HB class detection, a min_{MT} value, c_4, located in-between the mean values of the two classes of interest, i.e. "densely vegetated areas" and "low vegetation" has to be set. In Figure 5, where the min_{MT} boxplots for densely vegetated areas and bare soils, sparse/low vegetation classes are shown for all test cases, c_4 was fixed at -15dB. Based on the number of classes and their respective mean values, the following decision rules were defined:

i) if only one class is available and its min_{MT} mean value is higher than c_4, then all previously selected pixels are part of the class 'densely vegetated areas';

ii) if only one class is available and its min_{MT} mean value is lower than c_4, then all previously selected pixels are part of the class 'low vegetation';

iii) if two classes are available and their min_{MT} mean values are lower and higher than c_4, respectively, then all pixels belonging to the class with a PDF mean value lower than c_4 are removed using the HSBA;

iv) if two classes are available and their min_{MT} mean values are both lower or higher than c_4, then we are in the same situation as in points i) and ii).

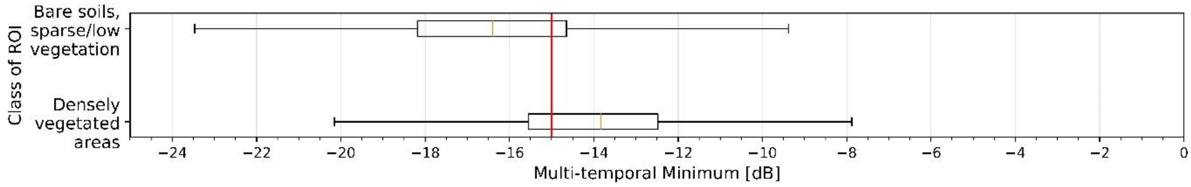

Figure 5 The multi-temporal minimum distribution of low vegetation and dense forest with the red vertical line showing the value of -15 dB. Pixels of each class were randomly selected based on a land cover map using 13 study cases.

3) The final step consists of merging the sublayers extracted in steps (1) and (2) in order to generate the EX-map.

It is worth pointing out that parameters c_1 , c_2 and c_4 are a priori values used to initialize/constrain the HSBA algorithm, while classes are identified automatically and adaptively. Consequently, in the entire procedure, the only parameter with a fixed value is c_3.

2.2. Sublayers of the EX-map

Besides the EX-map extraction, the individual sublayers of EX-maps such as permanent water bodies, layover (topographic) and shadow (topographic, urban) and arid areas provide essential information for many different EO applications. Therefore, the second objective of this study is to provide sublayers of the EX-map according to land cover types and different topography conditions.

Sublayers of LB class: As mentioned in Section 2.1.1, the LB class includes two sublayers, i.e. permanent water bodies sublayer and shadow (topographic, urban) and arid area. Based on the fact that the backscatter of permanent water bodies varies in the presence of wind, the permanent water bodies have much higher variations of temporal backscatter than the shadow (topographic, urban) and arid areas. Thus, permanent water bodies can be distinguished from shadow (topographic, urban) and arid areas based on the σ_{MT}, assuming that permanent water bodies have a Gaussian PDF with higher mean value with respect to the other two classes. The permanent water body class is selected using HSBA, assuming that the σ_{MT} distributions of water and non-water areas (i.e. shadow (topographic, urban) and arid areas) are two overlapped Gaussian distributions.

Sublayers of HB class: It has been defined that the HB class contains layover (topographic) and layover/double-bounce (urban). However, all these areas have similar backscatter behaviour, which makes it difficult to distinguish them using SAR intensity data. However, in order to distinguish HB pixels caused by high topography from urban areas, the local incidence angle (LIA) and the incidence angle from ellipsoid (INC) are computed using a DEM and the geometry of the SAR acquisition. The areas where the difference of INC and LIA is smaller than 5 degrees are regarded as layover/double-bounce (urban) areas while the other are pixels of layover (topographic) areas (Chini et al., 2018).

Sublayers of SB class: The SB class theoretically contains the areas with stable backscatter over time, such as shadow (topographic, urban) and arid areas, layover (topographic), layover/double-bounce (urban) and densely vegetated areas. However, the shadow (topographic, urban) and arid areas were identified in the previous steps as being part of the LB class, and the layover (topographic) and layover/double-bounce (urban) were previously classified as HB class. As a matter of fact, the SB class only contains densely vegetated areas.

3. Study areas and datasets

Six representative study sites located in four different continents were selected for testing and evaluating the proposed methodology. They are characterized by different land cover classes, different topographic conditions and different climates.

3.1. Study areas

Figure 6 depicts the location of the six study sites in four different continents. Three sites have been frequently affected by flood events in the years for which Sentinel-1 time series are available. For instance, study site 1, covering the plain of the River Severn (UK), is frequently hit by flood events, with a particularly high frequency in the period 2016 – 2018. Study site 3, focusing on the city of Beledweyne (Somalia), was also hit by frequent flooding between 2018 and 2020. Study site 6 covers the Houston area (US), which has frequently been impacted by the landfalls of hurricanes on the US South-eastern coast. Besides the areas affected by flooding, the other three test sites were considered relevant test cases as they exhibit land cover classes that are known to hamper the detection of floodwater using SAR intensity data. In particular, the identification of permanent low backscattering areas is very useful for flood mapping algorithms that use a single SAR image as input, as this allows distinguishing floodwater from permanent water bodies and water-lookalike surfaces. For example, study site 2, located in the Alps region close to Milan (Italy), was selected because it is composed of numerous topographic shadow and layover regions and, at the same time, contains many urbanized areas. Moreover, the region of Beijing (China) in study site 4 contains many small villages and settlements, while the study site 5 in the area around Wuhan (China) is characterized by a dense network of rivers and lakes, which are all land cover classes that are highly relevant for this study. In addition, the selection of test cases from markedly different regions across the world provides an opportunity to investigate the role of densely vegetated areas characterized by different vegetation types.

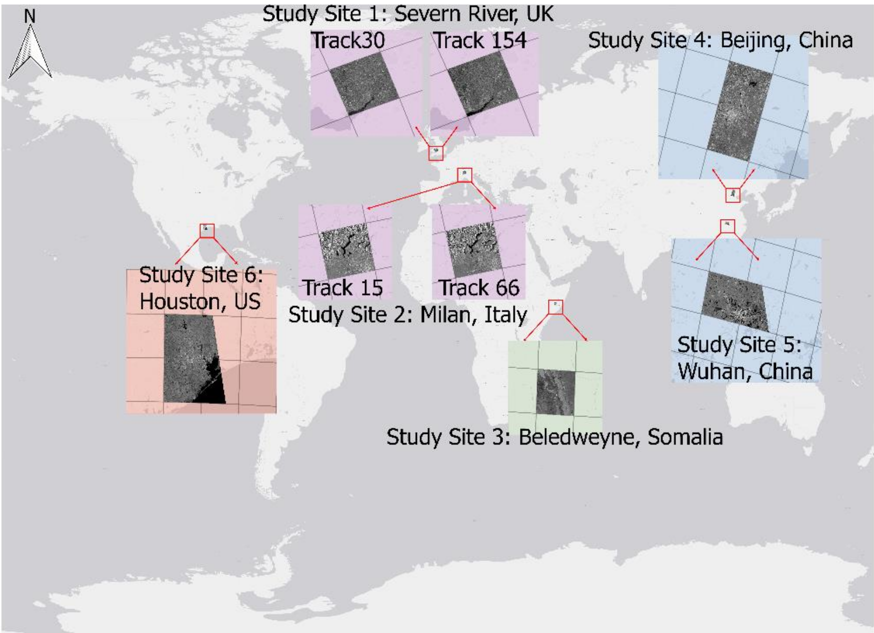

Figure 6 Study sites shown in global gall stereographic projection (EPSG: 54016). Different grid colours represent different projections in the Equi7Grid basic framework.

3.2. Sentinel-1 data

The Sentinel-1 dataset employed in this study is composed of multi-temporal images in Interferometric Wide Swath (IW) mode with VV polarization that were acquired between 2014 and 2019. All data were pre-processed and provided by the TU Wien Data Cube (Ali et al., 2017) for 13 different tiles of 100 × 100 km^2 and with a spatial resolution of 20 m. The data cube is managed and processed on the Earth Observation Data Centre (EODC) for Water Resources Monitoring. The EODC uses the high-performance computing platform provided by the third generation of the Vienna Scientific Cluster (VSC-3), providing easy access to EO data (Naeimi et al., 2016). In addition, EODC users can process EO data with their own algorithms and extract the results (Mathieu and Aubrecht, 2018). The Sentinel-1 data cube from TU Wien is derived by geocoding the SAR backscatter imagery using the python-based SAR Geophysical Retrieval Toolbox (SGRT), and the Sentinel-1 time-series from this data cube can be analysed directly in our study. The SAR datasets use the Equi7Grid projection (Bauer-Marschallinger et al., 2014) and all Sentinel-1 SAR data were split into 100 ×100 Km^2 tiles, as shown in Figure 6. Detailed information on the dataset is reported in Table 1.

Table 1 Detailed information of S1 IW data (D and A stand descending and ascending, respectively)

STUDY SITE	LOCATION	EQUI7GRID TILE	TRACK	PASS	ACQUISITION TIME	NUMBER OF IMAGES
1	River Severn, UK (Europe)	E040N023T1	30	A	2016.01.06 – 2018.12.03	215
		E040N023T1	154	D	2016.01.03 – 2018.12.24	282
2	Milan, Italy (Europe)	E046N014T1	15	A	2016.01.17 – 2018.12.26	167
		E046N014T1	66	D	2016.01.09 – 2019.01.05	258
3	Beledweyne, Somalia (Africa)	E082N056T1	35	D	2014.10.20 – 2019.12.17	161
4	Beijing, China (Asia)	E062N043T1	47	D	2016.01.19 – 2017.12.21	100
		E062N042T1				101
5	Wuhan, China (Asia)	E062N032T1	113	A	2016.01.24 – 2017.12.20	84
		E063N032T1				99
6	Houston, USA (North America)	E084N023T1	34	A	2016.04.12 – 2017.12.27	67
		E084N024T1				67
		E085N023T1				67
		E085N024T1				67

3.3. Evaluation dataset

Due to the uniqueness of the EX-map, there is no similar and independent map/mask currently available for validation. Thus, we propose to cross-compare the newly generated product with a map obtained from the ensemble of different datasets, hereafter referred to as the reference, that together approximate the content of the EX-map. Therefore, the reference map used for comparison is composed of those land cover classes and SAR image distortions that are expected to be part of the EX-map. We acknowledge that this does not allow for a complete quantitative evaluation, but rather for a qualitative evaluation of the results.

The reference is generated using globally available land cover maps derived from both passive and active Earth Observation data, including:

1) 30m FROM-GLC map derived from optical data (Gong et al., 2013), from which we have identified all classes that are supposed to be part of an EX-map;

2) shadow/layover map obtained through simulation using a DEM and the SAR acquisition geometry of each orbital track used in this study (Kropatsch and Strobl, 1990). It is worth noting that the 25m resolution DEM provided by Copernicus is used for European study sites 1 and 2 while the 30m SRTM DEM is used for the other study sites.

3) 12m resolution global urban footprint (GUF) data provided by DLR (Esch et al., 2018, 2017, 2011);

4) 20m resolution Sand Exclusion Layer (SEL) using the method proposed in (Martinis et al., 2018) (only involved for the evaluation of the EX-map in study site 3).

During the merging process of the four different sources of information, the layers derived from SAR data have higher priority than the land cover maps. The reference map was thus created starting with the layer of lowest priority and stratifying on top of all others. The hierarchy was decided based on the reliability of each product (i.e. GUF has a higher spatial resolution (i.e. 12m) than the 30m FROM-GLC map) and follows the listing of the four different layers given above, i.e. layer (1) having the lowest priority and layer (4) having the highest priority.

In addition, a 30m transition water map that is part of the global water surface map (Pekel et al., 2016) is also used for comparison with the water sublayer of the EX-map. However, it should be pointed out that the definition of our water sublayer and transition water are slightly different: our water sublayer includes water bodies, which can be derived from a multi-temporal median image (2014 to 2019) while the transition water map containing 10 surface water classes informs us of the change in seasonality between 1984 and 2015 (Pekel et al., 2016). Thus, only permanent, new permanent and seasonal-to-permanent water classes are considered for cross comparison.

4. Results and discussion

In this section, the EX-maps are evaluated using the reference map. Then, two EX-maps generated over the River Severn, UK (study site 1) and Beledweyne, Somalia (study site 3) are described and analysed in detail. Finally, the sublayers of the EX-map are evaluated with different reference datasets derived from the different data sources.

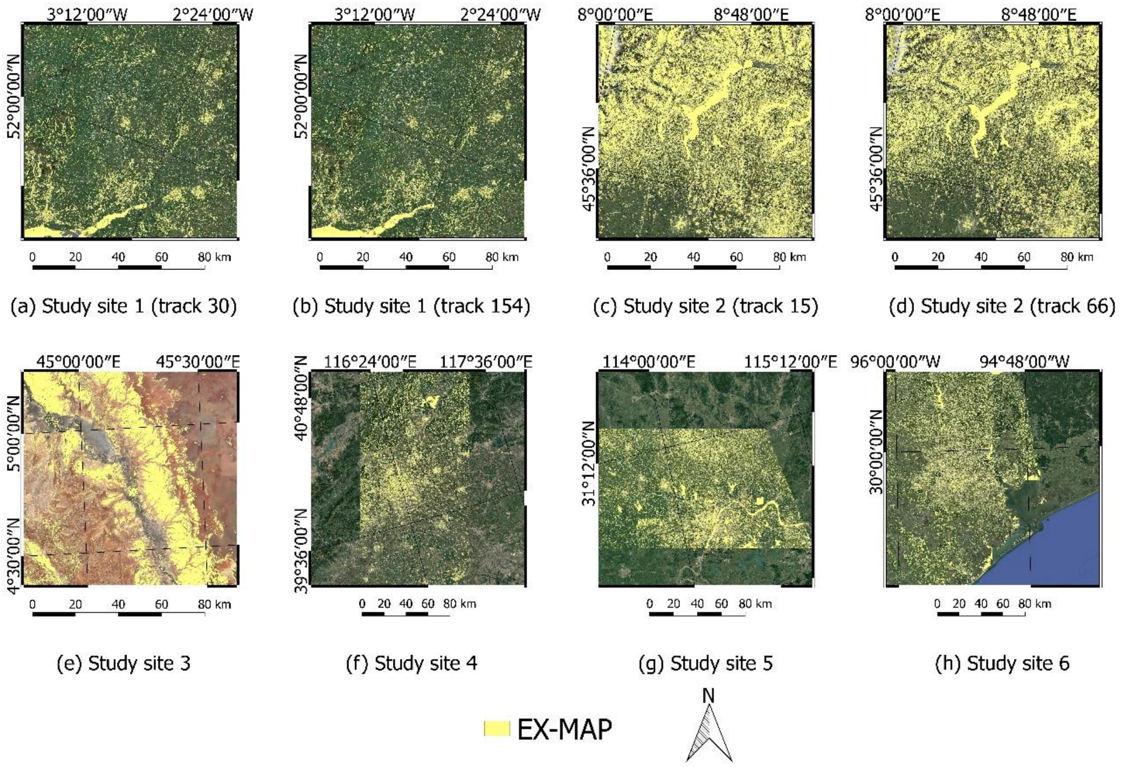

Figure 7 EX-maps from all study sites with the optical image from Google Earth as the background.

4.1. EX-map generation

The EX-maps generated over the 6 study sites are shown in Figure 7. In order to evaluate the quality of the EX-maps, the percentage of each land cover class in and outside the EX-map was plotted in Figure 8. According to our definition of the EX-map, and depending on the land cover classes available at the study sites, classes that are expected to be part of the EX-map are forest, water, impervious surface, layover, shadow, GUF, SEL and wetland, while those expected not to be part of the EX-map are cropland, grassland, shrubland, bare-land, snow/ice and tundra. As shown in Figure 8(a), for six orbital tracks, more than 68% of pixels included in the EX-maps are located in land cover classes that meet our definition of an EX-map. This percentage is expected to be high in exclusion areas, and low elsewhere. Indeed, with respect to areas not included in the EX-maps (Figure 8(b)), the majority of pixels belong to cropland, grassland and sparsely distributed shrubland for all study sites.

From Table 1, one can notice that the number of images varies from 67 to 282 while the time span varies from 20 months to 5 years for the different test sites. Although these differences exist in the dataset composition, the agreement between the EX-map and the expected land cover classes does not vary substantially. Test site 6 has the smallest number of images and a shorter time span but the EX-map performs as well as at site 2, which has a longer-term dataset. From these results, we can infer that datasets spanning more than one year, which is the common characteristic of all datasets used in this study, are necessary to extract a reliable EX-map. This guarantees the encompassing of pan-seasonal surface changes, which is the case for many vegetated areas. The satellite repeat cycle is also an important aspect to consider as a higher repeat cycle guarantees the possibility of having an exhaustive temporal statistic of backscattering values enabling the accurate sampling of all possible surface variations over time.

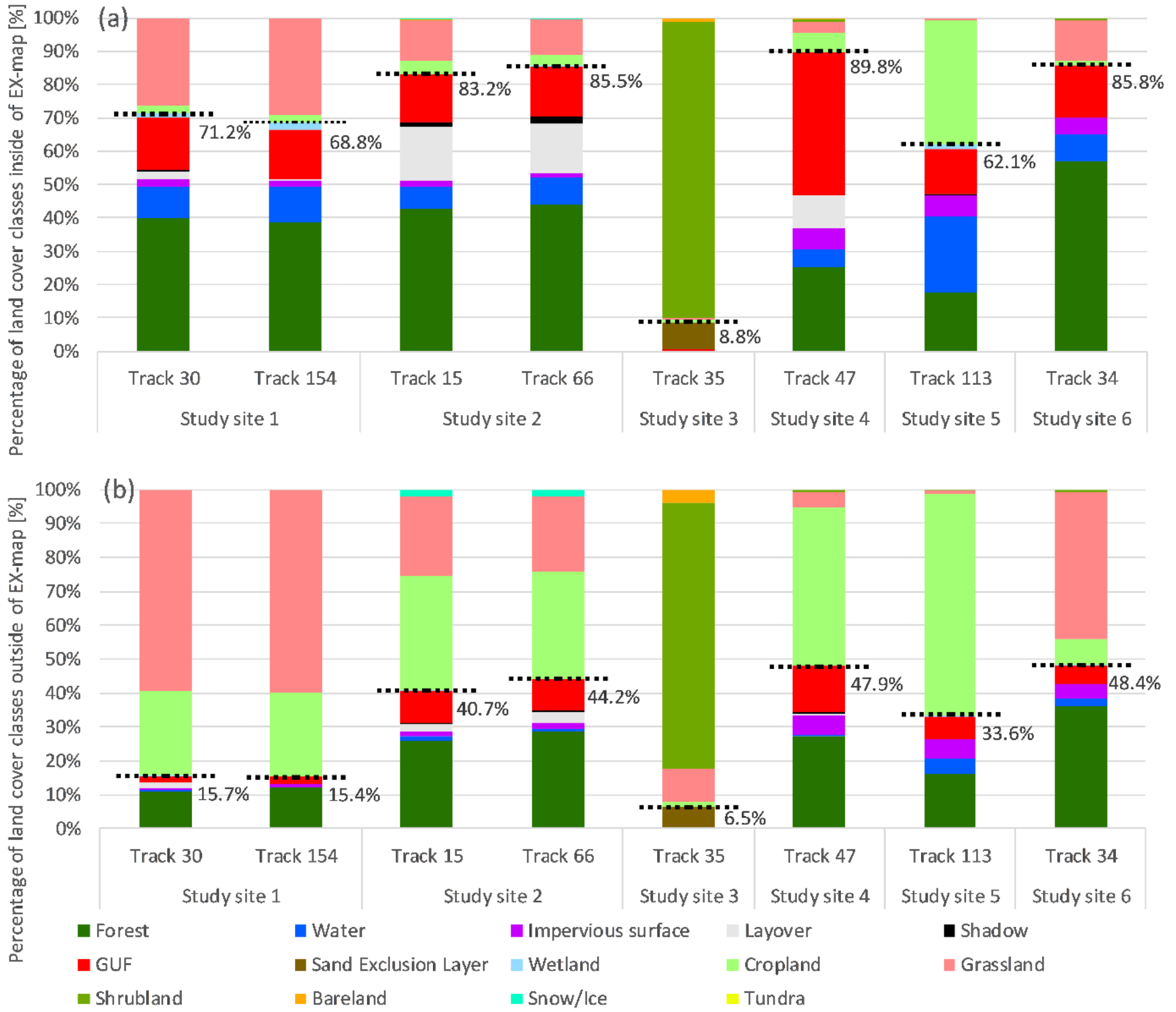

Figure 8 (a) Land cover classes of pixels included in the EX-map; (b) land cover classes of pixels outside the EX-map. The black dotted lines separate the classes expected to be inside the EX-map (below the black dotted line) and outside the EX-map (above the black dotted line); while the numbers indicate the percentage of pixels belonging to classes expected to be part of the EX-map in regions classified as an EX-map (a) or as not an EX-map (b).

Discrepancies between the two maps come from five main sources: errors in the EX-map, the difference in spatial resolution of the source data, difference in acquisition time of the images and reference maps, errors in the reference maps, as well as co-registration errors between different maps. We suspect the latter making an important contribution, especially on the boundaries of different land cover classes. Cropland and grassland are present in the EX-map, albeit at small percentages. This is probably caused by the presence of low-density tree areas that can be assigned to the EX-map, while they are assigned to cropland and grassland in the land cover map. Moreover, when using the 20 m resolution Sentinel-1 data, trees aligned along crop fields and several single trees near buildings are included in the EX-map due to their stable high temporal backscatter, while this level of detail is missing in the 30 m resolution global land cover maps. Furthermore, it is worth noting that the global-scale land cover map was derived from Landsat 5 TM and Landsat 7 ETM+ acquired between 1981 and 2011, with more than 70% of the Landsat data acquired after 2006 (Gong et al., 2013), while the Sentinel-1 data used in this study were acquired between 2014 and 2019. The difference in acquisition time may also lead to some inconsistencies between the two maps. At the Somalia test site, which is located in a region dominated by shrubland, the agreement between the EX-map and the reference is especially low and equal to 8.8% (Figure 8). This outlier will be discussed in Section 4.1.2. The forest class is also present outside the EX-map, which may be due to the presence of relatively low-density forest areas~~,~~ enabling the C-band signal to penetrate the canopy and to sense the ground surface.

We argue that the above-mentioned sources of discrepancy between the two maps also represent a point in favour of the proposed EX-map. This clearly shows that there is a necessity to consider an EX-map of areas where SAR-based intensity algorithms are unable to detect any changes, e.g. floodwater. In the following section, two test cases with large discrepancies between the EX-map and reference map are considered to gain a better understanding of the sources of the identified differences.

4.1.1. Study site 1: River Severn, UK

As shown in Figure 8 (a), about 28.8% of the pixels of the EX-map at study site 1 belong to grassland and cropland areas, which was not to be expected based on the definition of the EX-map. In order to have a better understanding of the differences between these two classes, we analyse very high resolution optical images from Google Earth to generate a new reference map

(Figure 9(e)). In the selected area in Figure 9(a), and according to the reference data shown in Figure 9(d), the EX-map (Figure 9(b)) should contain many grassland pixels. Instead, in the validation map obtained by visual inspection, many grassland pixels had been manually corrected to forest, thereby increasing the agreement with the EX-map. Two Confusion matrices from the EX-map using two different reference images are shown in Table 2. The overall accuracy (OA) and kappa coefficient of the generated EX-map using the manually derived reference image are 91.06% and 0.39, separately, while the overall accuracy and the kappa coefficient of the generated EX-map using the auxiliary products-derived reference image are 89.26% and 0.29. When looking at the numbers in this comparison, it is rather obvious that it is not possible to reach a perfect match between the two maps due to inherent differences in the two data sources. This demonstrates the necessity of deriving an EX-map from SAR data. One could argue that the greater these differences are, the more important it is to have a SAR-based EX-map.

It is worth noting that discrepancies are still present in the hilly areas indicated by the red box. High/low local $G_i$values (Figure 9(c)) seem to indicate that due to shadow and layover, no reliable SAR-based floodwater detection can be achieved in that area. However, according to the simulations carried out with the 25m DEM, no shadow or layover is to be expected from such gentle topography. As a result, no shadow or layover areas were included in the auxiliary products-derived reference map (Figure 9(d)).

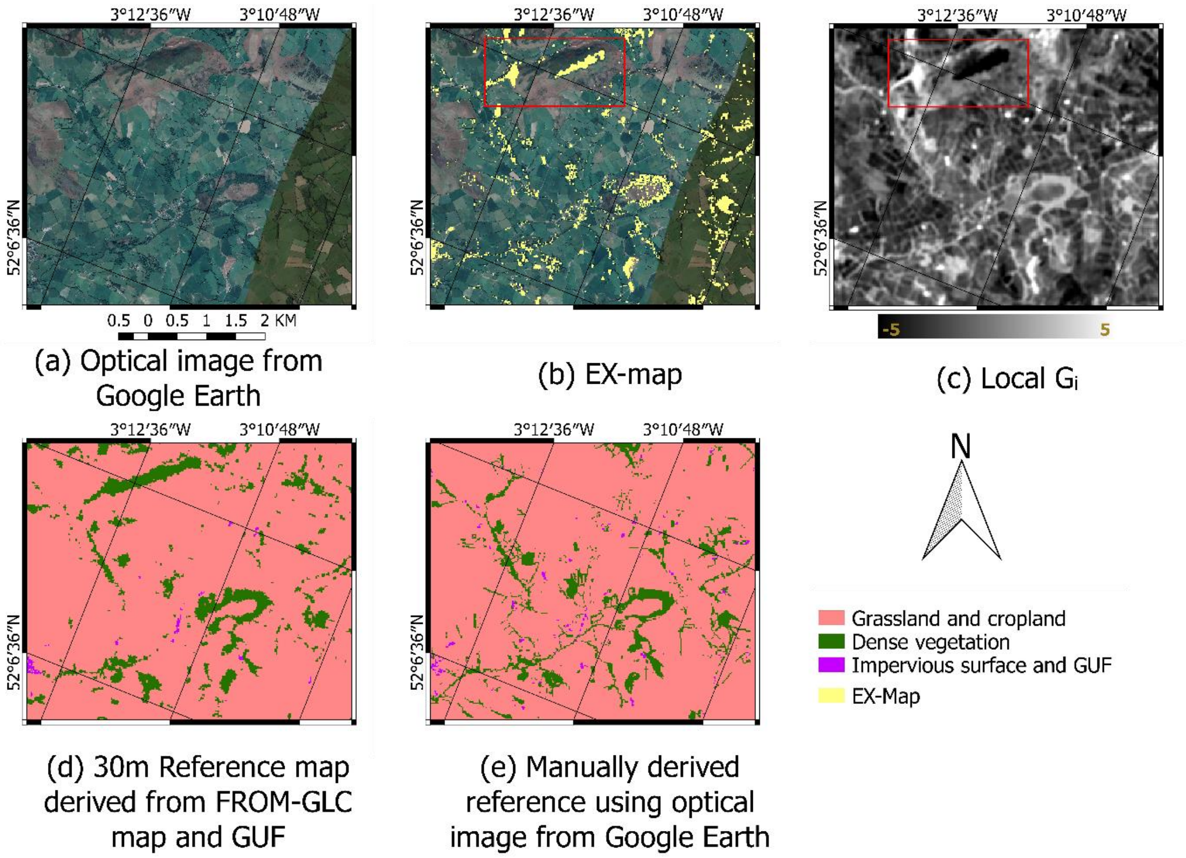

Figure 9 A subset of the EX-map derived from study site 1 (track30): grassland and cropland are shown in pink, dense vegetation is shown in green, impervious surface and GUF are shown in purple.

Table 2 Confusion matrix using 30m reference and manually derived reference: included class contains dense vegetation, impervious surface/GUF and shadow; excluded class contains grassland and cropland.

<table>
<tr><td colspan="2" rowspan="2">OA = 89.26%
Kappa = 0.29</td><td colspan="2">30m Reference</td><td colspan="2" rowspan="2">OA = 91.06%
Kappa = 0.39</td><td colspan="2">Manually derived Reference</td></tr>
<tr><td>Included</td><td>Excluded</td><td>Included</td><td>Excluded</td></tr>
<tr><td rowspan="2">EX-map</td><td>Included</td><td>1920</td><td>2310</td><td rowspan="2">EX-map</td><td>Included</td><td>2283</td><td>1947</td></tr>
<tr><td>Excluded</td><td>4766</td><td>56890</td><td>Excluded</td><td>3942</td><td>57714</td></tr>
</table>

4.1.2. Study site 3: Beledweyne, Somalia

Figure 8 (a) shows that 91.2% of the generated EX-map is composed of shrubland. This is surprising as we did not expect this class to be included in the EX-map. When considering the optical image in Figure 10 (a) and Figure 10 (b), there seem to be no densely vegetated areas hampering a SAR-based flood detection. The regions depicted in the red boxes are characterized by relatively high values of local G_i (Figure 10 (d)) and this is clearly the reason why the areas were included in the EX-map. From the SRTM DEM data shown in Figure 10 (e), it becomes apparent that these regions are marked by relatively high topographical variations resulting in higher temporal median backscatter and thus high local values of G_i. In other words, the shrublands are located in a region with high topographic variations and thus high local G_i values indicative of layover effects. The area of layover was not included in the reference map because the resolution of the SRTM was not sufficient to predict this effect. Furthermore, the visual inspection of the optical images of this area reveals that the shrub area is characterized by different types of soil or geology (Figure 11), some of which exhibit very high backscattering values and correspond to areas with higher topography. Our analysis suggests that the EX-map was indeed correctly extracted for this area. We would argue that this is a further confirmation of the necessity of generating an EX-map based on SAR time series analyses.

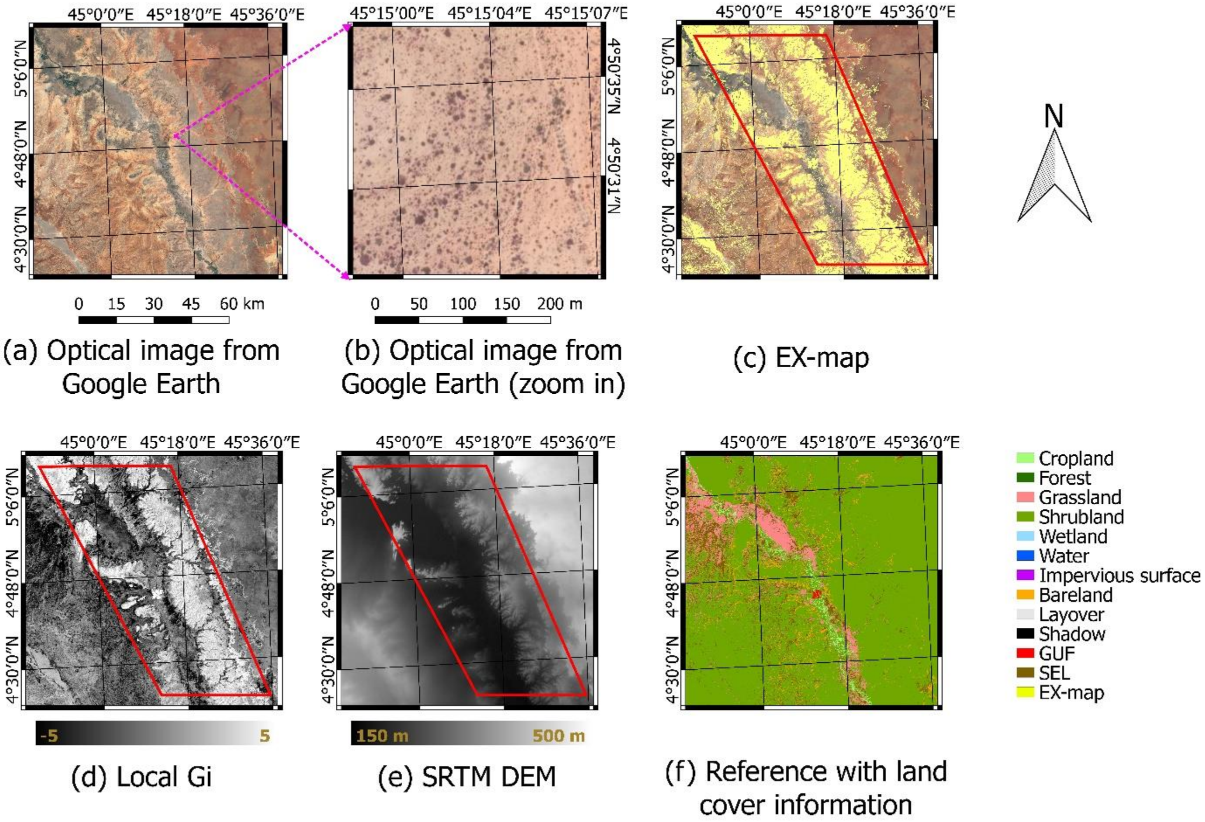

Figure 10 Input data sources, land cover classes and derived EX-map for study site 3 located in Beledweyne, Somalia. The scale of (c), (d), (e) and (f) are the same as (a).

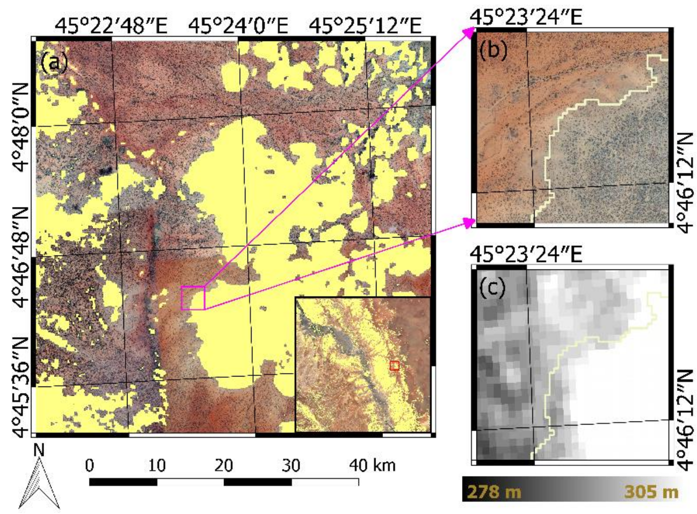

Figure 11 Example of shrubland with different soil types and elevation. (a) EX-map is shown in yellow with an optical image from Google Earth as background. (b) Zoom-in of an optical image from Google Earth. (c) 90m resolution STRM DEM corresponding to (b).

4.2. Evaluation of EX-map sublayers

The proposed method also provides a second layer of information, i.e. it splits the EX-map into five sublayers including shadow (topographic, urban) and arid areas, permanent water bodies, layover (topographic), layover/double-bounces (urban) and densely vegetated areas. In this section, the accuracy of four of the five sublayers is evaluated using different reference data sets, taking the kappa coefficient and the OA as performance measures. In particular, water is compared with the 30m global surface water map (Pekel et al., 2016), layover/double-bounce (urban) is evaluated using the 12m resolution GUF data, while layover (topographic) and shadow (topographic, urban) and arid areas are assessed using the layover/shadow masks derived by means of a DEM considering the geometrical characteristic of the specific SAR acquisition orbit and SEL extracted from SAR time-series (Martinis et al., 2018). Regarding the sublayer of the densely vegetated areas, it was not possible to evaluate it because this sublayer is rather unique and no similar reference data set was available. The permanent water bodies sublayer was evaluated at all test sites, except in Beledweyne (Somalia) because no permanent water bodies were classified in that region. Kappa coefficients higher than 0.6 and the OAs higher than 0.9 for all test sites (Table 3) indicate that the permanent water bodies sublayer generated is reliable.

Table 3 Evaluation results of selected sublayers in the EX-map generated at different study sites (study site is abbreviated to SS in this table)

	PERMANENT WATER BODIES		**LAYOVER (TOPOGRAPHIC)**		**SHADOW (TOPOGRAPHIC, URBAN) AND ARID AREAS**		**LAYOVER/DOUBLE-BOUNCE (URBAN)**	
	Kappa	OA	Kappa	OA	Kappa	OA	Kappa	OA
SS1_TRACK 30	0.76	0.99	-	-	-	-	0.34	0.96
SS1_TRACK 154	0.83	0.99	-	-	-	-	0.23	0.96

SS2_TRACK 15	0.96	1.00	0.69	0.94	0.24	0.99	0.21	0.88
SS2_TRACK 66	0.95	1.00	0.66	0.95	0.29	0.98	0.13	0.88
SS3	-	-	-	-	0.48	0.95	0.01	0.78
SS4	0.68	0.99	-	-	-	-	0.15	0.82
SS5	0.62	0.96	-	-	-	-	0.22	0.93
SS6	0.82	0.99	-	-	-	-	0.18	0.95

Sublayers representing layover (topographic) and shadow (topographic, urban) and arid areas were only evaluated on the Italian and Somalia sites, as they are the only two sites with significant mountainous (i.e. the Alps) and arid areas. This allows for the extraction of consistent shadow and layover masks by means of a DEM and SEL mask using time-series of SAR data. In fact, the layover and shadow caused by low topography could be missed entirely due to the rather low resolution of DEMs. As shown in Table 3, the layover (topographic) sublayer matches the reference layover reasonably well. The kappa coefficient is higher than 0.6 and OA is higher than 0.9. On the other hand, the shadow (topographic, urban) and arid areas sublayer correspond poorly with the shadow mask from the DEM and SEL since the kappa coefficients are 0.24, 0.29 and 0.48 for the three different tracks. The low kappa coefficient values are arguably caused by inaccurate DEM-derived shadow masks and different definitions of arid areas. Indeed, a more in-depth analysis of the results reveals that the shadow areas extracted from the DEM largely underestimate the actual SAR shadow areas. This becomes apparent in Figure 12, where the EX-map shadow (topographic, urban) and arid areas sublayer and the reference shadow mask generated by DEM are shown in blue and yellow, respectively, while the area where the two layers overlap is depicted in red. The visual inspection of the SAR temporal median backscattering image highlights that low backscattering values over mountainous regions, i.e. shadow, overlap well with the EX-map shadow (topographic, urban) and arid areas sub-layer, while this is not the case for the DEM-based shadow mask. This is further confirmed by calculating the average of the temporal median backscattering values within pixels belonging to the EX-map and DEM-based shadow. The values are -20 dB and -13 dB, respectively, where -20 dB can be considered more realistic for the shadow (topographic, urban) and arid areas class than -13 dB. Therefore, we argue that the shadow (topographic, urban) and arid areas sublayer provided by the generated EX-map outperforms the DEM-derived shadow mask due to the relatively low resolution of the DEM.

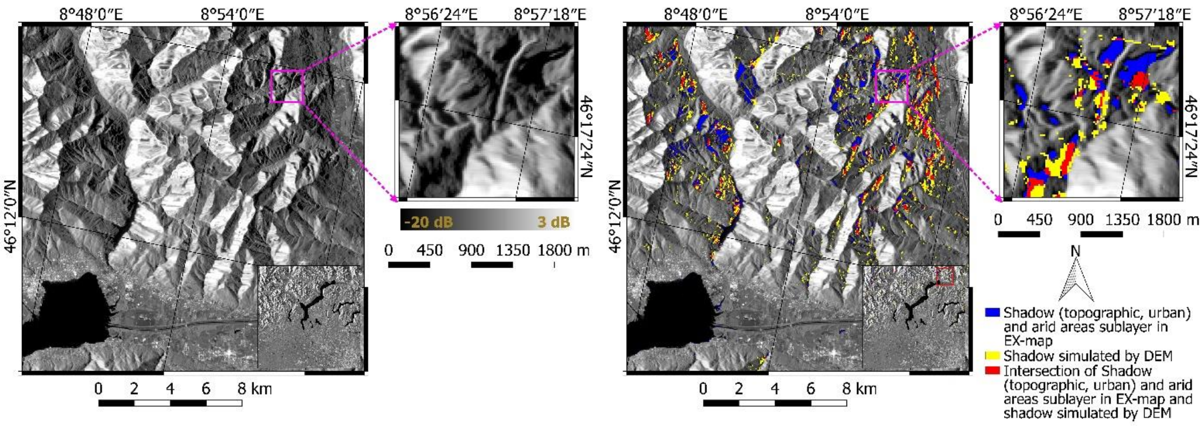

Figure 12 Example of a shadow sublayer in the EX-map and a reference shadow mask: shadow sublayers in blue, reference shadow mask in yellow and the overlapped areas of shadow sublayer and reference shadow mask in red. Background is temporal median image.

With respect to layover/double bounce (urban) sublayers in the EX-map, the kappa is quite low when using GUF as reference data while OAs are very high (Table 3). The low value of the kappa coefficient could be explained by the fact that, while the EX-map urban sublayer represents only layover/double-bounce from buildings (high values of backscattering), the GUF also contains other targets, such as car parks, gardens, etc. An example of this is shown in Figure 13.

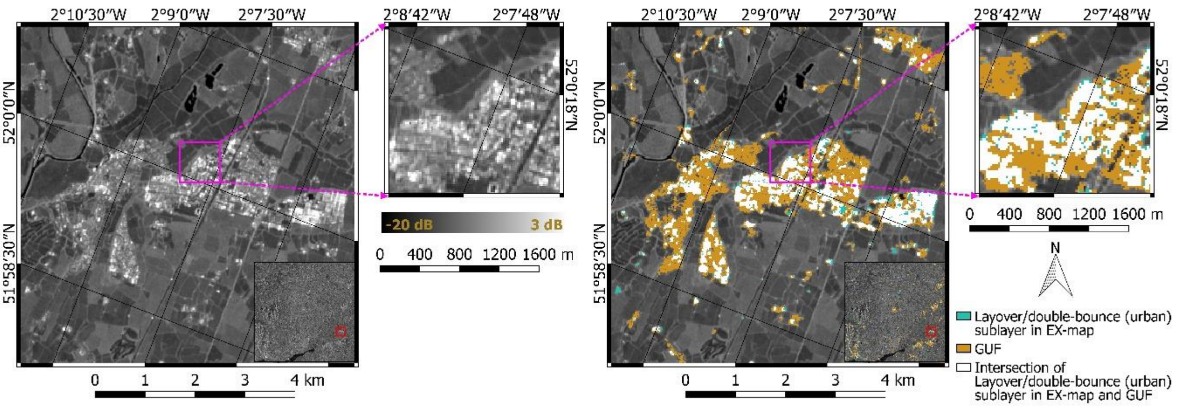

Figure 13 Example of layover/double-bounce (urban) sublayer in the EX-map and reference urban mask (GUF). Green shows only the layover/double-bounce (urban) sublayer in the EX-map, ginger, only the GUF and white, the intersection of the layover/double-bounce (urban) sublayer in the EX-map and the GUF. The background is the multi-temporal median image.

The validation of each sublayer has been useful to evaluate the quality and reliability of each sublayer and, at the same, to assess the EX-map itself.

5. Applications of the EX-map

In this section, the EX-map is applied and tested in the context of floodwater mapping. For three different test cases, flood extent maps obtained through SAR-based change detection and the associated EX-maps are extracted from SAR time series analyses. The three flood events here considered are: a) the River Severn and the city of Tewkesbury (UK), on 11 February 2016; b) the Webi Shebelle River and the city of Beledweyne (Somalia) on 6 May 2018; c) Hurricane Harvey-related flooding in the metropolitan area of Houston (USA), on 30 August 2017. For all three events, the floodwater maps were obtained via the change detection approach proposed in Chini et al., (2017) using Sentinel-1 images from the same orbits that were used for generating the EX-maps. Moreover, the flooding in Houston was mapped using the methods described in Chini et al. (2018, 2019). Finally, we briefly describe an idea for using the EX-map in hydrological models.

5.1. Case of the River Severn flood (UK), 11 February 2016

The flood image was acquired on 11 February 2016 during the flood event and the reference image was acquired on 24 January 2017 after the flood. As shown in Figure 14, the HSBA-derived flood extent map is represented in blue and the generated EX-map is displayed in yellow. This example indicates that there is hardly any overlap between the EX-map and the flood extent map obtained. However, a small overlapping area depicted in red covers permanent water bodies that were not removed by change detection, probably due to wind affecting one of the two image acquisitions. In general, it can be observed that many exclusion pixels are located in the vicinity of the floodwater. This result, in particular, highlights the importance of complementing the flood extent maps with an EX-map, as it informs end users of areas where no classification of floodwater is possible. An interesting example of this is the zoom-in box in Figure 14, depicting the town of Tewkesbury, which is prone to flooding (Giustarini et al., 2013) and largely included in the EX-map.

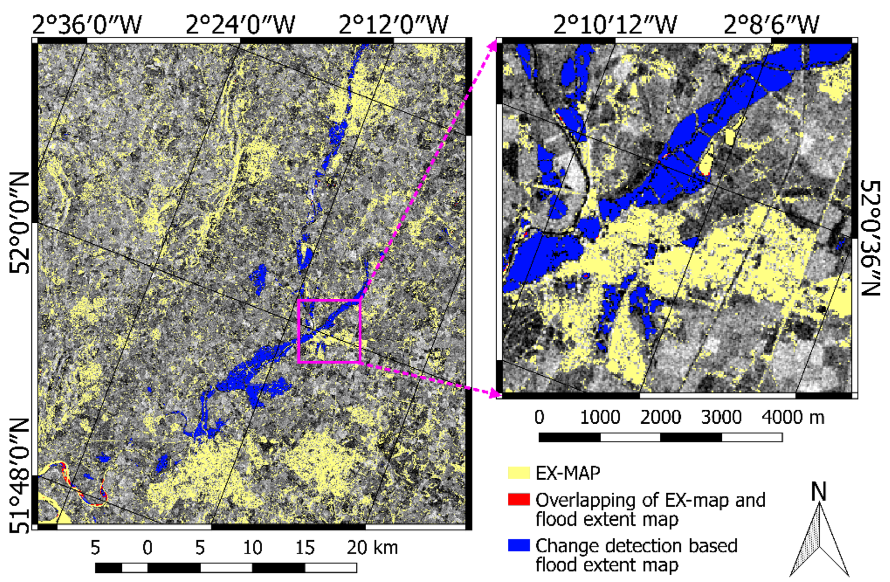

Figure 14 Change detection-based flood map and EX-map of the River Severn, UK.

5.2. Case of the Beledweyne flood (Somalia), 6 May 2018

As a second case study, we selected a flooding of the Webi Shebelle River, which occurred in the region of the city of Beledweyne, Somalia on 6 May 2018. A Sentinel-1 IW image acquired on 8 May 2018 is used as the flood image while an image acquired on 13 May 2017 is considered as the reference image. In Figure 15 (a), the extent of the EX-map and floodwater map is shown in yellow and blue, respectively, while the overlapping area is indicated in red. For this event, a flood extent map provided by UNITAR (https://unitar.org/unosat/node/44/2796) is considered as an independent reference data set. It was manually derived using Radarsat-2 and cloud-free optical data acquired on 9 May 2018. The availability of this dataset provides some further insights on the usefulness of the EX-map (Figure 15(b)). In Figure 15(b), pixels in violet identify areas with an overlap between the EX-map and the UNITAR floodwater map. The overlapping areas are mostly located in urban areas (red box). Moreover, the under-detected floodwater areas in the black box (Figure 15(b)) are also part of the EX-map. Following the observation of Martinis et al. (2018), these areas are characterized by a stable, permanently low backscatter of around -20 dB that is not significantly impacted by the appearance of floodwater. Moreover, Table 4 shows the confusion matrix computed on the UNITAR flood map and intensity change detection-based flood map with and without considering the EX-map. The OA increases from 95.92% to 97.02% and the kappa coefficient increases from 0.40 to 0.48 when considering the EX-map. It can be argued that this result is further evidence of the added value of the EX-map for stakeholders in flood management.

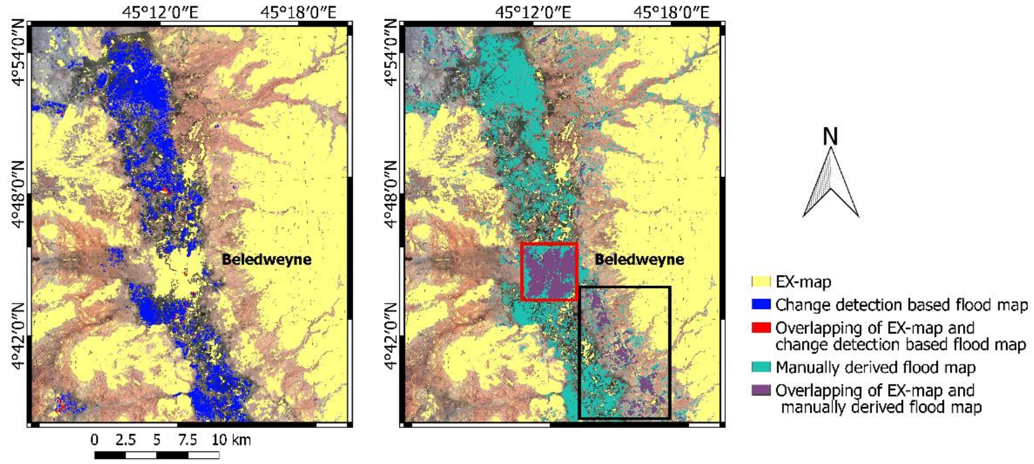

(a) Comparison between EX-map and change detection based flood map

(b) Comparison between EX-map and manually derived flood map

Figure 15 Comparison of the EX-map with a change detection-based flood extent map and flood extent reference in Beledweyne, Somalia.

Table 4 Confusion matrix using a change detection-based flood map and manually derived reference map, applying and not applying the EX-map.

<table>
<tr><td colspan="2" rowspan="2">OA = 95.92%
Kappa = 0.40</td><td colspan="2">Manually derived flood map</td><td colspan="2" rowspan="2">OA = 97.02%
Kappa = 0.48</td><td colspan="2">Manually derived flood map using EX-map</td></tr>
<tr><td>Flood</td><td>No flood</td><td>Flood</td><td>No flood</td></tr>
<tr><td rowspan="2">Change detection-based flood map</td><td>Flood</td><td>357217</td><td>165388</td><td rowspan="2">Change detection-based flood map using EX-map</td><td>Flood</td><td>352754</td><td>160601</td></tr>
<tr><td>No flood</td><td>820034</td><td>22822361</td><td>No flood</td><td>60282</td><td>23091363</td></tr>
</table>

5.3. Case of the Houston flood (USA), 29 August 2017

As a third case study, we selected the Hurricane Harvey-related flooding in the metropolitan area of Houston in August 2017. In this case, the EX-map was compared with the SAR-based floodwater extracted using not only the SAR intensity (Chini et al., 2017) (Figure 16 (a)) but also the InSAR coherence (Chini et al., 2019) (Figure 16 (b)). In Figure 16 (a), pixels in yellow and blue represent non-overlapping regions of the EX-map and the SAR intensity-based flood map (i.e. mainly flooded regions over open areas), while pixels in red represent the overlapping part. The small number of pixels in red are located on the edge of the EX-map and are probably due to an underlying mixture of different land cover classes. Moreover, Figure 16 (b) provides the comparison between the EX-map and the floodwater map that is derived from InSAR coherence, in addition to SAR intensity data. The advanced mapping approach means that the flood extent map includes both flooded open areas and a significant part of flooded buildings. Pixels in green indicate the urban flood map, and pixels in violet represent the overlap between the EX-map and the urban flood map. As shown in Figure 16 (b), the high number of pixels in violet represent the flooded buildings that could only be identified by considering InSAR coherence in addition to SAR intensity data. This result supports our initial assumption that an EX-map provides essential additional information for SAR intensity-based flood maps.

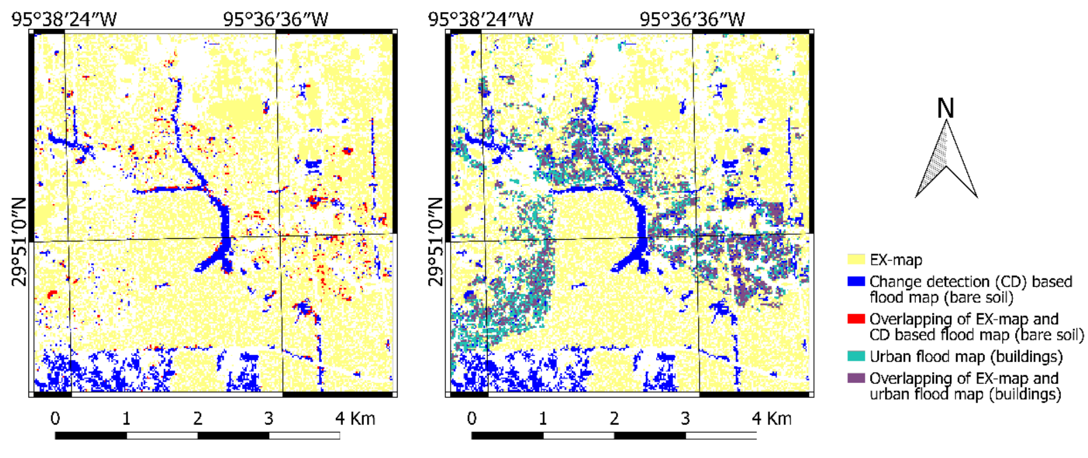

(a) Comparison between EX-map and change detection flood map (bare soils)

(b) Comparison between EX-map and urban flood map (buildings)

Figure 16 Comparison of the EX-map with a change detection-based flood extent map and urban flood extent using InSAR coherence in Houston, USA.

5.4. Assimilating the EX-map in hydrological-shallow water models

Hydrodynamic models are powerful tools for simulating and predicting flood inundations. Besides the different input data (e.g. precipitation, streamflow, DEM) that are necessary for running these models, there is a need for additional data to enable the reduction of their prediction uncertainty. In this context, the assimilation of SAR data into flood forecasting models has proven its value for reducing the uncertainties (Cooper et al., 2019; Dasgupta et al., 2021a, 2021b; Di Mauro et al., 2021.). However, Di Mauro et al. (2021) also shows that the effectiveness of the assimilation of SAR-derived flood maps into a flood forecasting model significantly drops when there are significant errors in the observation. Prior to the assimilation it is therefore of primary importance to mask out areas where the SAR observations do not provide any reliable information on the flood situation. As a matter of fact, our EX-maps are expected to provide relevant information for increasing the performance of the assimilation. In this way, SAR information is assimilated only in the areas outside EX-maps while other auxiliary data can be analysed in the areas included in EX-maps.

6. Conclusions

In this study, we introduced an automatic approach for generating an exclusion map, i.e. EX-map representing areas that cannot be classified as flooded or unflooded using SAR intensity data. We argue that the generation of an EX-map is of paramount importance when mapping floodwater using SAR intensity-based approaches. To this end, the EX-map includes shadow and layover caused by mountains/buildings, sand areas, permanent water bodies and densely vegetated areas. To obtain this map, we proposed an automatic method using three temporal/spatial indicators, namely the local Getis-Ord G_i computed using the multi-temporal median backscatter, multi-temporal minimum and multi-temporal standard deviation~~,~~ extracted from the C-Band Sentinel-1 IW SAR time series from the EODC data-cube. While previous methods use masks derived from auxiliary datasets, our EX-map is exclusively derived from time series of SAR data. It is therefore better tailored to data that are also used to extract the floodwater extent. Moreover, the proposed method provides five valuable EX-map sublayers representing specific land cover and SAR image distortion classes. The sublayer information could also be used to remove the layover/double-bounce (urban) sublayer from the EX-map for algorithms enabling the detection of floodwater in urban areas based on multitemporal InSAR coherence (Chini et al., 2019; Pulvirenti et al., 2021).

The proposed method was tested and evaluated on 6 study sites using Sentinel-1 IW images with a spatial resolution of 20 m that were acquired from eight orbital tracks. The quality of the EX-map was evaluated by a cross-comparison with globally available land cover maps. The observed discrepancies between the EX-map and the dataset used for cross-comparison are mainly located in densely vegetated areas (i.e. dense forests) and urban areas affected by layover/double-bounce. They can be largely explained by inherent differences in the definition between the EX-map and reference dataset. We argue that the definition of the EX-map is more appropriate than the ones of other reference datasets when dealing with SAR-based retrievals. Moreover, the analysis of the second informative layer, i.e. the five EX-map sublayers, supports our conclusion: the layover areas caused by topography and permanent water bodies were covered by the EX-map with satisfying accuracy, i.e. the kappa coefficients and OAs were higher than 0.6; the shadow (topographic, urban) and arid areas in the EX-map were better classified compared to the DEM-derived shadow mask and SEL and the layover/double-bounce (urban) sublayer in the EX-map only included the layover/double-bounce areas in built-up environments. The EX-map still shows limitations in the low vegetation areas (e.g. grassland, cropland and shrubland), because in some regions, low vegetation with a stable backscatter behaviour over time, is difficult to distinguish from the densely vegetated areas.

The usefulness and effectiveness of this new product are further tested in the framework of three different flood events occurring in different parts of the world. The results provide evidence that the EX-map highlights most of the areas affected by classification errors, demonstrating that the EX-map adds value to flood extent maps obtained with conventional SAR-based flood mapping methods.

It can be argued that besides complementing flood mapping, the proposed EX-map may also support the assimilation of flood extent maps into hydrological-hydraulic models. In the next step, the proposed EX-map will therefore be applied to mask out areas that should not be considered when assimilating SAR-based flood extent observations into hydrological-shallow water models. Other applications of EX-map are planned to be investigated. Indeed, we hypothesize that the availability of EX-MAP has the potential to support different geophysical parameter retrievals relying on backscattering intensity, e.g. soil moisture.

Acknowledgment

This work is supported by the Luxembourg National Research Fund (FNR) through the HYDRO-CSI project (reference: FNR PRIDE HYDRO-CSI 10623093). Wolfgang Wagner acknowledges funding from the Austrian Space Applications Programme (FFG Project 878946 ACube4Floods). The thoughtful comments from the three anonymous reviewers and editors are greatly appreciated and helped enhance the final version of the article.

Reference

Ali, I., Naeimi, V., Cao, S., Elefante, S., Le, T., Bauer-Marschallinger, B., Wagner, W., 2017.

Sentinel-1 data cube exploitation: Tools, products, services and quality control, in: 2017 Conference on Big Data from Space. https://doi.org/10.2760/383579

Bauer-Marschallinger, B., Freeman, V., Cao, S., Paulik, C., Schaufler, S., Stachl, T., Modanesi, S., Massari, C., Ciabatta, L., Brocca, L., Wagner, W., 2019. Toward Global Soil Moisture Monitoring With Sentinel-1: Harnessing Assets and Overcoming Obstacles. IEEE Trans. Geosci. Remote Sens. 57, 520–539. https://doi.org/10.1109/TGRS.2018.2858004

Bauer-Marschallinger, B., Sabel, D., Wagner, W., 2014. Optimisation of global grids for high-resolution remote sensing data. Comput. Geosci. 72, 84–93. https://doi.org/10.1016/j.cageo.2014.07.005

Benoudjit, A., Guida, R., 2019. A Novel Fully Automated Mapping of the Flood Extent on SAR Images Using a Supervised Classifier. Remote Sens. 11, 779. https://doi.org/10.3390/rs11070779

Chen, X., Sun, Q., Hu, J., 2018. Generation of Complete SAR Geometric Distortion Maps Based on DEM and Neighbor Gradient Algorithm. Appl. Sci. 8, 2206. https://doi.org/10.3390/app8112206

Chini, M., Hostache, R., Giustarini, L., Matgen, P., 2017. A Hierarchical Split-Based Approach for Parametric Thresholding of SAR Images: Flood Inundation as a Test Case. IEEE Trans. Geosci. Remote Sens. 55, 6975–6988. https://doi.org/10.1109/TGRS.2017.2737664

Chini, M., Pelich, R., Hostache, R., Matgen, P., Lopez-Martinez, C., 2018. Towards a 20 m Global Building Map from Sentinel-1 SAR Data. Remote Sens. 10, 1833. https://doi.org/10.3390/rs10111833

Chini, M., Pelich, R., Pulvirenti, L., Pierdicca, N., Hostache, R., Matgen, P., 2019. Sentinel-1 InSAR Coherence to Detect Floodwater in Urban Areas: Houston and Hurricane Harvey as A Test Case. Remote Sens. 11, 107. https://doi.org/10.3390/rs11020107

Cian, F., Marconcini, M., Ceccato, P., 2018. Normalized Difference Flood Index for rapid flood mapping: Taking advantage of EO big data. Remote Sens. Environ. 209, 712–730. https://doi.org/10.1016/j.rse.2018.03.006

Clauss, K., Ottinger, M., Leinenkugel, P., Kuenzer, C., 2018. Estimating rice production in the Mekong Delta, Vietnam, utilizing time series of Sentinel-1 SAR data. Int. J. Appl. Earth Obs. Geoinf. 73, 574–585. https://doi.org/10.1016/j.jag.2018.07.022

Cooper, E.S., Dance, S.L., García-Pintado, J., Nichols, N.K., Smith, P.J., 2019. Observation operators for assimilation of satellite observations in fluvial inundation forecasting. Hydrol. Earth Syst. Sci. 23, 2541–2559. https://doi.org/10.5194/hess-23-2541-2019

CRED UNISDR, 2015. The Human Cost of Weather-related Disasters 1995-2015.

Dasgupta, A., Hostache, R., Ramsankaran, R., Schumann, G.J.P., Grimaldi, S., Pauwels, V.R.N., Walker, J.P., 2021a. On the Impacts of Observation Location, Timing, and Frequency on Flood Extent Assimilation Performance. Water Resour. Res. 57. https://doi.org/10.1029/2020WR028238

Dasgupta, A., Hostache, R., Ramsankaran, R., Schumann, G.J.P., Grimaldi, S., Pauwels, V.R.N., Walker, J.P., 2021b. A Mutual Information-Based Likelihood Function for Particle Filter Flood Extent Assimilation. Water Resour. Res. 57. https://doi.org/10.1029/2020WR027859

Debusscher, B., Van Coillie, F., 2019. Object-Based Flood Analysis Using a Graph-Based Representation. Remote Sens. 11, 1883. https://doi.org/10.3390/rs11161883

Di Mauro, C., Hostache, R., Matgen, P., Pelich, R., Chini, M., Leeuwen, J. Van, Nichols, N., Blöschl, G., 2021. Assimilation of probabilistic flood maps from SAR data into a hydrologic-hydraulic forecasting model : a proof of concept. Hydrol. Earth Syst. Sci. https://doi.org/https://doi.org/10.5194/hess-2020-403

Esch, T., Bachofer, F., Heldens, W., Hirner, A., Marconcini, M., Palacios-Lopez, D., Roth, A., Üreyen, S., Zeidler, J., Dech, S., Gorelick, N., 2018. Where We Live—A Summary of the Achievements and Planned Evolution of the Global Urban Footprint. Remote Sens. 10, 895. https://doi.org/10.3390/rs10060895

Esch, T., Heldens, W., Hirner, A., Keil, M., Marconcini, M., Roth, A., Zeidler, J., Dech, S., Strano, E.,

2017. Breaking new ground in mapping human settlements from space – The Global Urban Footprint. ISPRS J. Photogramm. Remote Sens. 134, 30–42. https://doi.org/10.1016/j.isprsjprs.2017.10.012

Esch, T., Schenk, A., Ullmann, T., Thiel, M., Roth, A., Dech, S., 2011. Characterization of Land Cover Types in TerraSAR-X Images by Combined Analysis of Speckle Statistics and Intensity Information. IEEE Trans. Geosci. Remote Sens. 49, 1911–1925. https://doi.org/10.1109/TGRS.2010.2091644

Ferro, A., Brunner, D., Bruzzone, L., Lemoine, G., 2011. On the relationship between double bounce and the orientation of buildings in VHR SAR images. IEEE Geosci. Remote Sens. Lett. 8, 612–616. https://doi.org/10.1109/LGRS.2010.2097580

Franceschetti, G., Iodice, A., Riccio, D., 2002. A canonical problem in electromagnetic backscattering from buildings. IEEE Trans. Geosci. Remote Sens. 40, 1787–1801. https://doi.org/10.1109/TGRS.2002.802459

Gamba, P., Aldrighi, M., Stasolla, M., Sirtori, E., 2009. A detailed comparison between two fast approaches to urban extent extraction in VHR SAR images, in: 2009 Joint Urban Remote Sensing Event. IEEE, pp. 1–6. https://doi.org/10.1109/URS.2009.5137592

Getis, A., Ord, J.K., 1992. The Analysis of Spatial Association by Use of Distance Statistics. Geogr. Anal. 24, 189–206. https://doi.org/10.1111/j.1538-4632.1992.tb00261.x

Giustarini, L., Hostache, R., Kavetski, D., Chini, M., Corato, G., Schlaffer, S., Matgen, P., 2016. Probabilistic Flood Mapping Using Synthetic Aperture Radar Data. IEEE Trans. Geosci. Remote Sens. 54, 6958–6969. https://doi.org/10.1109/TGRS.2016.2592951

Giustarini, L., Hostache, R., Matgen, P., Schumann, G.J.P., Bates, P.D., Mason, D.C., 2013. A Change Detection Approach to Flood Mapping in Urban Areas Using TerraSAR-X. IEEE Trans. Geosci. Remote Sens. 51, 2417–2430. https://doi.org/10.1109/TGRS.2012.2210901

Gong, P., Wang, J., Yu, L., Zhao, Y., Zhao, Y., Liang, L., Niu, Z., Huang, X., Fu, H., Liu, S., Li, C., Li, X., Fu, W., Liu, C., Xu, Y., Wang, X., Cheng, Q., Hu, L., Yao, W., Zhang, H., Zhu, P., Zhao, Z., Zhang, H., Zheng, Y., Ji, L., Zhang, Y., Chen, H., Yan, A., Guo, J., Yu, L., Wang, L., Liu, X., Shi, T., Zhu, M., Chen, Y., Yang, G., Tang, P., Xu, B., Giri, C., Clinton, N., Zhu, Z., Chen, J., Chen, J., 2013. Finer resolution observation and monitoring of global land cover: first mapping results with Landsat TM and ETM+ data. Int. J. Remote Sens. 34, 2607–2654. https://doi.org/10.1080/01431161.2012.748992

Grimaldi, S., Xu, J., Li, Y., Pauwels, V.R.N., Walker, J.P., 2020. Flood mapping under vegetation using single SAR acquisitions. Remote Sens. Environ. 237, 111582. https://doi.org/10.1016/j.rse.2019.111582

Hostache, R., Chini, M., Giustarini, L., Neal, J., Kavetski, D., Wood, M., Corato, G., Pelich, R., Matgen, P., 2018. Near-Real-Time Assimilation of SAR-Derived Flood Maps for Improving Flood Forecasts. Water Resour. Res. 54, 5516–5535. https://doi.org/10.1029/2017WR022205

Huang, C., Nguyen, B.D., Zhang, S., Cao, S., Wagner, W., 2017. A Comparison of Terrain Indices toward Their Ability in Assisting Surface Water Mapping from Sentinel-1 Data. ISPRS Int. J. Geo-Information 6, 140. https://doi.org/10.3390/ijgi6050140

Kropatsch, W.G., Strobl, D., 1990. The generation of SAR layover and shadow maps from digital elevation models. IEEE Trans. Geosci. Remote Sens. 28, 98–107. https://doi.org/10.1109/36.45752

Landuyt, L., Van Wesemael, A., Schumann, G.J.P., Hostache, R., Verhoest, N.E.C., Van Coillie, F.M.B., 2019. Flood Mapping Based on Synthetic Aperture Radar: An Assessment of Established Approaches. IEEE Trans. Geosci. Remote Sens. 57, 722–739. https://doi.org/10.1109/TGRS.2018.2860054

Li, Y., Martinis, S., Plank, S., Ludwig, R., 2018. An automatic change detection approach for rapid flood mapping in Sentinel-1 SAR data. Int. J. Appl. Earth Obs. Geoinf. 73, 123–135. https://doi.org/10.1016/j.jag.2018.05.023

Li, Y., Martinis, S., Wieland, M., 2019a. Urban flood mapping with an active self-learning convolutional neural network based on TerraSAR-X intensity and interferometric coherence. ISPRS J. Photogramm. Remote Sens. 152, 178–191. https://doi.org/10.1016/j.isprsjprs.2019.04.014

Li, Y., Martinis, S., Wieland, M., Schlaffer, S., Natsuaki, R., 2019b. Urban Flood Mapping Using SAR Intensity and Interferometric Coherence via Bayesian Network Fusion. Remote Sens. 11, 2231. https://doi.org/10.3390/rs11192231

Liang, J., Liu, D., 2020. A local thresholding approach to flood water delineation using Sentinel-1 SAR imagery. ISPRS J. Photogramm. Remote Sens. 159, 53–62. https://doi.org/10.1016/j.isprsjprs.2019.10.017

Lin, K.-F., Perissin, D., 2018. Single-Polarized SAR Classification Based on a Multi-Temporal Image Stack. Remote Sens. 10, 1087. https://doi.org/10.3390/rs10071087

Martinis, S., Plank, S., Ćwik, K., 2018. The Use of Sentinel-1 Time-Series Data to Improve Flood Monitoring in Arid Areas. Remote Sens. 10, 583. https://doi.org/10.3390/rs10040583

Mason, D.C., Dance, S.L., Vetra-Carvalho, S., Cloke, H.L., 2018. Robust algorithm for detecting floodwater in urban areas using synthetic aperture radar images. J. Appl. Remote Sens. 12, 1. https://doi.org/10.1117/1.jrs.12.045011

Matgen, P., Martinis, S., Wagner, W., Freeman, V., Zeil, P., McCormick, N., 2019. Feasibility assessment of an automated, global, satellite-based flood-monitoring product for the Copernicus Emergency Management Service., European Commission, Ispra. https://doi.org/10.2760/653891

Mathieu, P., Aubrecht, C., 2018. Earth Observation Open Science and Innovation, Earth Observation Open Science and Innovation. Springer International Publishing, Cham. https://doi.org/10.1007/978-3-319-65633-5

Naeimi, V., Wagner, W., Elefante, S., Dostalova, A., Cao, S., Bauer-Marschallinger, B., 2016. Geophysical Parameters Retrieval From Sentinel-1 Sar Data: A Case Study For High

Performance Computing At EODC, in: 24th High Performance Computing Symposium. Society for Modeling and Simulation International (SCS), pp. 68–75. https://doi.org/10.22360/SpringSim.2016.HPC.026

Natsuaki, R., Nagai, H., 2020. Synthetic Aperture Radar Flood Detection under Multiple Modes and Multiple Orbit Conditions: A Case Study in Japan on Typhoon Hagibis, 2019. Remote Sens. 12, 903. https://doi.org/10.3390/rs12060903

Nobre, A.D., Cuartas, L.A., Hodnett, M., Rennó, C.D., Rodrigues, G., Silveira, A., Waterloo, M., Saleska, S., 2011. Height Above the Nearest Drainage – a hydrologically relevant new terrain model. J. Hydrol. 404, 13–29. https://doi.org/10.1016/j.jhydrol.2011.03.051

Ord, J.K., Getis, A., 1995. Local Spatial Autocorrelation Statistics: Distributional Issues and an Application. Geogr. Anal. 27, 286–306. https://doi.org/10.1111/j.1538-4632.1995.tb00912.x

Panteras, G., Cervone, G., 2018. Enhancing the temporal resolution of satellite-based flood extent generation using crowdsourced data for disaster monitoring. Int. J. Remote Sens. 39, 1459–1474. https://doi.org/10.1080/01431161.2017.1400193

Pekel, J.F., Cottam, A., Gorelick, N., Belward, A.S., 2016. High-resolution mapping of global surface water and its long-term changes. Nature 540, 418–422. https://doi.org/10.1038/nature20584

Pierdicca, N., Pulvirenti, L., Chini, M., 2018. Flood Monitoring through Remote Sensing. https://doi.org/10.1007/978-3-319-63959-8

Pulvirenti, L., Chini, M., Pierdicca, N., 2021. InSAR Multitemporal Data over Persistent Scatterers to Detect Floodwater in Urban Areas: A Case Study in Beletweyne, Somalia. Remote Sens. 13, 37. https://doi.org/10.3390/rs13010037

Pulvirenti, L., Chini, M., Pierdicca, N., Boni, G., 2016. Use of SAR Data for Detecting Floodwater in Urban and Agricultural Areas: The Role of the Interferometric Coherence. IEEE Trans. Geosci. Remote Sens. 54, 1532–1544. https://doi.org/10.1109/TGRS.2015.2482001

Schlaffer, S., Chini, M., Giustarini, L., Matgen, P., 2017. Probabilistic mapping of flood-induced backscatter changes in SAR time series. Int. J. Appl. Earth Obs. Geoinf. 56, 77–87. https://doi.org/10.1016/j.jag.2016.12.003

Schlaffer, S., Matgen, P., Hollaus, M., Wagner, W., 2015. Flood detection from multi-temporal SAR data using harmonic analysis and change detection. Int. J. Appl. Earth Obs. Geoinf. 38, 15–24. https://doi.org/10.1016/j.jag.2014.12.001

Shen, X., Wang, D., Mao, K., Anagnostou, E., Hong, Y., 2019. Inundation Extent Mapping by Synthetic Aperture Radar: A Review. Remote Sens. 11, 879. https://doi.org/10.3390/rs11070879

Songchitruksa, P., Zeng, X., 2010. Getis–Ord Spatial Statistics to Identify Hot Spots by Using Incident Management Data. Transp. Res. Rec. J. Transp. Res. Board 2165, 42–51. https://doi.org/10.3141/2165-05

Tran, D.X., Pla, F., Latorre-Carmona, P., Myint, S.W., Caetano, M., Kieu, H. V., 2017. Characterizing the relationship between land use land cover change and land surface temperature. ISPRS J. Photogramm. Remote Sens. 124, 119–132. https://doi.org/10.1016/j.isprsjprs.2017.01.001

Tsyganskaya, V., Martinis, S., Marzahn, P., Ludwig, R., 2018a. SAR-based detection of flooded vegetation – a review of characteristics and approaches. Int. J. Remote Sens. 39, 2255–2293. https://doi.org/10.1080/01431161.2017.1420938

Tsyganskaya, V., Martinis, S., Marzahn, P., Ludwig, R., 2018b. Detection of temporary flooded vegetation using Sentinel-1 time series data. Remote Sens. 10. https://doi.org/10.3390/rs10081286

Ulaby, F.T., Long, D.F., 2014. Microwave Radar and Radiometric Remote Sensing. United States of America: University of Michigan Press.

Wagner, W., Freeman, V., Cao, S., Matgen, P., Chini, M., Salamon, P., McCormick, N., Martinis, S., Bauer-Marschallinger, B., Navacchi, C., Schramm, M., Reimer, C., Briese, C., 2020. DATA PROCESSING ARCHITECTURES FOR MONITORING FLOODS USING SENTINEL-1. ISPRS Ann. Photogramm. Remote Sens. Spat. Inf. Sci. V-3-2020, 641–648.

https://doi.org/10.5194/isprs-annals-V-3-2020-641-2020

Westerhoff, R.S., Kleuskens, M.P.H., Winsemius, H.C., Huizinga, H.J., Brakenridge, G.R., Bishop, C., 2013. Automated global water mapping based on wide-swath orbital synthetic-aperture radar. Hydrol. Earth Syst. Sci. 17, 651–663. https://doi.org/10.5194/hess-17-651-2013

Wood, M., Hostache, R., Neal, J., Wagener, T., Giustarini, L., Chini, M., Corato, G., Matgen, P., Bates, P., 2016. Calibration of channel depth and friction parameters in the LISFLOOD-FP hydraulic model using medium-resolution SAR data and identifiability techniques. Hydrol. Earth Syst. Sci. 20, 4983–4997. https://doi.org/10.5194/hess-20-4983-2016

Wulder, M., Boots, B., 1998. Local spatial autocorrelation characteristics of remotely sensed imagery assessed with the Getis statistic. Int. J. Remote Sens. 19, 2223–2231. https://doi.org/10.1080/014311698214983

Zhao, J., Chini, M., Matgen, P., Hostache, R., Pelich, R., Wagner, W., 2019. An Automatic SAR-Based Change Detection Method for Generating Large-Scale Flood Data Records: The UK as a Test Case, in: IGARSS 2019 - 2019 IEEE International Geoscience and Remote Sensing Symposium. IEEE, pp. 6138–6141. https://doi.org/10.1109/IGARSS.2019.8900534

Zhao, J., Pelich, R., Hostache, R., Matgen, P., Wagner, W., Chini, M., 2021. A large-scale 2005–2012 flood map record derived from ENVISAT-ASAR data: United Kingdom as a test case. Remote Sens. Environ. 256, 112338. https://doi.org/10.1016/j.rse.2021.112338